Coarsening dynamics can explain meiotic crossover patterning in both the presence and absence of the synaptonemal complex

John A Fozard[1], Chris Morgan[2,*], Martin Howard[1,*]

[1] Computational and Systems Biology and [2]Cell and Developmental Biology, John Innes Centre, Norwich Research Park, Norwich NR4 7UH, UK

* Co-corresponding authors: chris.morgan@jic.ac.uk, martin.howard@jic.ac.uk

Abstract

The shuffling of genetic material facilitated by meiotic crossovers is a critical driver of genetic variation. Therefore, the number and positions of crossover events must be carefully controlled. In *Arabidopsis,* an obligate crossover and repression of nearby crossovers on each chromosome pair are abolished in mutants that lack the synaptonemal complex (SC), a conserved protein scaffold. We use mathematical modelling and quantitative super-resolution microscopy to explore and mechanistically explain meiotic crossover pattering in *Arabidopsis* lines with full, incomplete or abolished synapsis. For *zyp1* mutants, which lack an SC, we develop a coarsening model in which crossover precursors globally compete for a limited pool of the pro-crossover factor HEI10, with dynamic HEI10 exchange mediated through the nucleoplasm. We demonstrate that this model is capable of quantitatively reproducing and predicting *zyp1* experimental crossover patterning and HEI10 foci intensity data. Additionally, we find that a model combining both SC- and nucleoplasm-mediated coarsening can explain crossover patterning in wild-type *Arabidopsis* and in *pch2* mutants, which display partial synapsis. Together, our results reveal that regulation of crossover patterning in wild-type *Arabidopsis* and SC defective mutants likely act through the same underlying coarsening mechanism, differing only in the spatial compartments through which the pro-crossover factor diffuses.

Introduction

During meiotic prophase I, pairs of threadlike homologous chromosomes are tethered together through the formation of a protein scaffold called the synaptonemal complex (SC) (Page and Hawley, 2004). Prior to SC formation, programmed double strand breaks (DSBs) form along the length of the chromosomal DNA (Gray and Cohen, 2016; Hunter, 2015). DSBs are then repaired via the formation of recombination-intermediate (RI) DNA joint-molecules, as either non-crossovers (NCOs) or crossovers (COs) (Gray and Cohen, 2016; Hunter, 2015). In most species, the number of RIs repaired as NCOs vastly outnumbers those repaired as COs (Gray and Cohen, 2016; Hunter, 2015). Importantly, nearby pairs of COs on the same chromosome are less likely to occur than more distant pairs, but each pair of chromosomes always receives at least one CO. These phenomena are known as 'crossover interference' and 'crossover assurance', respectively (Jones and Franklin, 2006; Otto and Payseur, 2019; Sturtevant, 1915; von Diezmann and Rog, 2021; Zickler and Kleckner, 2016).

Recently, we introduced a mechanistic coarsening model that quantitatively explains CO interference, CO assurance and other CO patterning features in wild-type *Arabidopsis thaliana* (Morgan et al., 2021). In our SC-mediated coarsening model, the pro-CO protein HEI10 (Chelysheva et al., 2012; Ziolkowski et al., 2017) can diffuse along synapsed homolog bivalents and can reversibly bind into immobile clusters at RI sites. Conservation of the total amount of HEI10 on individual bivalents, along with an unbinding escape rate from RIs that decreases as more HEI10 locally accumulates, causes the system to coarsen. By the end of the pachytene substage of prophase I, significant amounts of HEI10 are retained at only a small number of predominantly distantly-spaced RIs, each with high levels of HEI10, which are then designated to become COs (Morgan et al., 2021). A similar model was subsequently proposed to underlie CO patterning in *C. elegans* (Zhang et al., 2021), suggesting that this molecular coarsening paradigm represents a conserved feature of meiotic CO control.

The coarsening model fundamentally relies on the retention of HEI10 molecules on synapsed bivalent chromosomes, and redistribution of HEI10 molecules by diffusion along the bivalents. Work in *C. elegans* points to the SC acting as a conduit, or channel, through which HEI10 molecules can diffuse, promoting coarsening along individual bivalents. Consistently, in *C. elegans*, the SC is known to have liquid-crystal like properties that can spatially compartmentalise pro-CO proteins (Rog et al., 2017; Zhang et al., 2018). Furthermore, innovative live-cell imaging experiments have recently directly demonstrated that ZHP-3, a HEI10 ortholog, can diffuse along the SC (Stauffer et al., 2019; Zhang et al., 2021). In *Arabidopsis*, it was also recently shown that CO interference and assurance are abolished in plants lacking the SC transverse filament protein, ZYP1 (Capilla-Pérez et al., 2021; France et al., 2021). These observations suggest that the SC plays a direct role in mediating crossover patterning dynamics.

In this work, we therefore develop a new coarsening model for crossover interference in the absence of an SC, and use it to explore the regulation of crossover number and position in *Arabidopsis zyp1* mutants with abolished synapsis. In this new model, due to the lack of an SC, HEI10 molecules are no longer restricted to diffuse along individual bivalents. Instead, HEI10 is assumed to diffuse through a communal nucleoplasm, generating competition for HEI10 between RIs located on different bivalents. Similarly, in *C. elegans*, it has previously been suggested that the SC functions to prevent exchange of recombination proteins between RIs via the nucleoplasm (Rog et al., 2017; Zhang et al., 2021, 2018). Other studies have also recently proposed that nucleoplasm-mediated coarsening can explain CO patterning in *Arabidopsis* mutants with abolished synapsis, although the dynamics of this process have not been explicitly modelled (Durand et al., 2022; Lloyd, 2022). Using

our model, we provide a mechanistic explanation for why *zyp1* mutants without synapsis lose both CO interference and assurance. Intriguingly, we also reveal and explain an additional layer of crossover control, where *zyp1* mutants lose positional effects that are determined by CO interference along individual chromosome pairs, but still exhibit constraints on total crossover number per-cell. Importantly, we also find that a model combining nucleoplasm-mediated and SC-mediated coarsening is still fully capable of explaining CO patterning in wild-type *Arabidopsis,* as well as in *pch2* mutants, which display incomplete synapsis (Lambing et al., 2015). Overall, our results demonstrate a critical role for the SC in controlling and constraining the dynamic coarsening of HEI10 molecules.

Results

A nucleoplasm-mediated coarsening model for crossover patterning without the SC

The SC likely acts as a conduit for HEI10 diffusion along synapsed pachytene bivalents (Morgan et al., 2021; Rog et al., 2017; Zhang et al., 2021, 2018). Without an SC, we postulated that HEI10 diffusion could instead occur through the nucleoplasm, with little or no movement along chromosomes, as has also previously been suggested from work in *C. elegans* (Zhang et al., 2021). We therefore investigated this hypothesis by developing a new coarsening model for crossover interference without an SC. This 'nucleoplasmic coarsening' model incorporates the processes shown in Figure 1A,B on the 5 pairs of homologous chromosomes in each cell, whose lengths are drawn from the experimentally measured length distributions, and with randomly positioned recombination intermediates (RIs) (Methods).

In this model, HEI10 is able to move from the nucleoplasmic pool to the HEI10 clusters at each of the RIs. It can also escape from the RI clusters back into the nucleoplasmic pool, at a rate which depends on the amount of HEI10 within that RI cluster. Similar to previous work (Morgan et al., 2021), this rate is chosen to have the form shown in Figure 1C,D, decreasing as the amount of HEI10 within the RI compartment increases. Again, as in our earlier model (Morgan et al., 2021), if the total amount of HEI10 is sufficiently high then a uniform steady state becomes unstable and the system progressively coarsens, with RIs with more HEI10 growing at the expense of those with less. Eventually, the majority of the HEI10 will accumulate into a single focus per cell, but the limited duration of pachytene means that this process does not complete, and instead there are a number of RIs with significant levels of HEI10 at the end of the simulation. Full details of the simulated model can be found in Figure 1A-G and Methods, including minor differences in how the model was simulated (in the initial distribution of HEI10, dynamics at small HEI10 foci and criteria for HEI10 focus/CO calling) as compared to our earlier work (Morgan et al., 2021).

Nucleoplasmic coarsening model explains CO number distribution in *zyp1* mutants

To determine whether the nucleoplasmic coarsening model was capable of explaining CO patterning in *Arabidopsis* mutants without synapsis, we first manually adjusted model parameter values to fit simulation outputs to existing experimental data on CO frequency from *Arabidopsis zyp1* null mutants, which lack an SC. These data include total CO number and number of homologs without a CO (Figure 2A,B).

By counting the number of MLH1 foci in late-prophase I cells in 7 different Col-0 *zyp1* null mutant lines, it was previously found that there was a ~50% increase in the predominant class I COs in these mutants compared with wild-type (data from (Capilla-Pérez et al., 2021), shown in Figure 2A). Also, by analysing DAPI stained metaphase I cells, it was found that ~11% of metaphase I cells contained a

115 pair of univalent chromosomes, which form when homologs fail to form a single CO, indicating an
116 absence of CO assurance (data from (Capilla-Pérez et al., 2021), shown in Figure 2B). Importantly, we
117 found that the nucleoplasmic coarsening model was capable of recapitulating the increase in CO
118 number and the increased univalent frequency observed in *zyp1* mutants (Figure 2A, B). The number
119 of COs per cell was slightly less dispersed, with a lower sample variance, within our model than in
120 the experimental data. This reduction is likely because the experimental data is pooled from multiple
121 different mutant lines, each of which has a slightly different mean number of COs per cell, thereby
122 generating a broader distribution (Capilla-Pérez et al., 2021). The expected frequency of univalents is
123 also slightly higher in our simulation outputs than in the experimental data, but this is again
124 expected as chiasma number in metaphase I cells (that were used for the experimental analysis) are
125 influenced by both class I and class II CO numbers, whereas the nucleoplasmic coarsening model
126 only simulates CO patterning via the (dominant) class I pathway. Assuming ~2 additional class II COs
127 per cell (Mercier et al., 2005) are distributed randomly among the five chromosome pairs, in a
128 simple estimation we would expect the univalent frequency in our model output to be reduced by a
129 factor of $(0.8)^2$=0.64 (from 19% of cells to 12% of cells containing one or more univalent). However,
130 univalents are more likely to be associated with the shorter chromosomes, as they have fewer RIs.
131 This was recently experimentally demonstrated, with chromosome 4 (the shortest *Arabidopsis*
132 chromosome) exhibiting the highest frequency of aneuploidy in *zyp1* mutants (Durand et al., 2022).
133 This effect slightly reduces how much the addition of class II crossovers decreases the frequency of
134 cells with one or more univalent. In our simulations we thus find a value of ~13%, similar to but
135 slightly higher than previous observations (~11%) (Capilla-Pérez et al., 2021).

136 Using the nucleoplasmic coarsening model, we were also able to simulate the distribution of
137 crossovers on each of the five *Arabidopsis* chromosomes (Figure 2C). Consistent with previous
138 genetic analyses, we found that the average number of crossovers per chromosome pair is positively
139 correlated with their physical size (Durand et al., 2022). We also found that the distribution of the
140 number of crossovers on each chromosome is close to a Poisson distribution, with nearly equal
141 mean and variance. Processes that occur at a constant probability per unit space or time, when
142 integrated over a fixed interval, have a Poisson distribution (Haldane, 1931). Hence, as expected, CO-
143 interference along each chromosome is not present in this model. These findings are consistent with
144 a previous genetic analysis, which found that the distribution of CO numbers on individual
145 chromosomes did not deviate from a Poisson distribution (Capilla-Pérez et al., 2021).

146 Paradoxically, while the distribution of CO numbers on individual chromosomes in our simulations
147 closely followed a Poisson distribution, the total number of COs per cell did not. Applying a test for
148 underdispersion (Cameron and Trivedi, 1990), the distribution of simulated CO numbers was found
149 to be significantly under-dispersed relative to a Poisson distribution ($z=-276.85$, $p<0.001$, see also
150 Figure 2A). Compellingly, we found that a sub-Poissonian distribution of total CO numbers per cell
151 was also found in the experimental data from (Capilla-Pérez et al., 2021) (Figure 2A; test for
152 underdispersion $z=-6.5757$, $p<0.001$), although this experimental under-dispersion was not
153 previously highlighted. In the model, the total number of crossovers in each cell is regulated through
154 global competition for a limited pool of HEI10. This, combined with regulation of cell-to-cell total
155 HEI10 amounts (Methods) leads to under-dispersion, despite the fact that there is little or no control
156 on the number of crossovers on each chromosome pair. This under-dispersion persists in the model
157 even with altered initial conditions (eliminating non-uniform initial HEI10 loading, Methods, Figure 2
158 – figure supplement 1).

159 We also found that the coarsening dynamics within the nucleoplasmic coarsening model were
160 capable of producing the experimentally observed final CO numbers within the limited ~10h

duration of the pachytene substage of prophase I in *Arabidopsis* (Prusicki et al., 2019) (Figure 2D). Overall, we find that the nucleoplasmic coarsening model fits well with prior data on CO numbers in SC mutants, giving strong support to the hypothesis of nucleoplasmic HEI10 exchange.

Nucleoplasmic coarsening model explains CO number distribution in *zyp1* HEI10 overexpressing mutants

To further test the ability of the nucleoplasmic coarsening model to explain CO patterning in mutants without synapsis, we also sought to fit the model to recent experimental data examining the combined effect of *zyp1* loss of function and HEI10 overexpression (Durand et al., 2022). Again, by counting the number of MLH1 foci in late-prophase cells it was found that combining the *zyp1* mutation with HEI10 overexpression leads to an average of 45.0 (σ^2=64) class I COs per cell in male Col-0 meiocytes (Durand et al., 2022). This represents an increase in class I COs to approximately 3.5 times the number in wild-type. Unlike in the sole *zyp1* mutant, there was no evidence of a sub-Poissonian distribution of COs per cell within the *zyp1* + HEI10 overexpression lines (test for underdispersion; z=1.0843, p=0.86).

Increasing the total HEI10 within our nucleoplasmic coarsening model to 3.5 times its original amount (applied to both the mean and standard-deviation of the distribution of total cellular HEI10) gave approximately the same increase in CO number (to mean CO number 47.3), but did not generate the observed increase in variance (σ^2 = 14), which was significantly smaller than the experimental observations (Levene's test for equality of variances F(1,10034)=68.602, p<0.001). To obtain increased variance in CO number, we increased the standard-deviation in the total cellular HEI10 levels, increasing by approximately an order of magnitude (Methods). With this additional noise, which we attribute to presence of the HEI10 transgene, we were able to recapitulate this experimentally observed increase in CO number and variance, with simulation outputs giving an average of 46.9 COs per cell (σ^2 = 63), this variance not being significantly different (F(1,10034)=0.0982, p=0.754).

Super-resolution imaging of HEI10 in SC-defective *zyp1* mutant cells

As described above, previous studies have used HEI10 and MLH1 focus counts per cell, alongside genetic analyses, to examine the effects of SC absence on CO frequency in *Arabidopsis.* However, the material positioning of recombination sites (in units of microns) along prophase I chromosomes has not yet been cytologically investigated in *zyp1* mutants. This is particularly important because, as argued in (Zickler and Kleckner, 2016), the optimal metric for measuring CO interference is microns of axis length. Additionally, as shown previously, correlations between HEI10 focal intensity and foci number or position can be detected that provide strong experimental support for the coarsening model (Morgan et al., 2021).

We therefore used super-resolution microscopy and a bespoke image-analysis pipeline to quantify the position and intensity of late-HEI10 foci (that are known to mark the positions of class I COs (Chelysheva et al., 2012)), along late prophase I chromosomes in wild-type and *zyp1a-2/zyp1b-1* SC null mutant lines (previously characterised in (France et al., 2021)) (Figure 3A,B). Late-prophase I cells from wild-type and *zyp1a-2/zyp1b-1* plants were stained for SMC3 (Lam et al., 2005) and HEI10 (Chelysheva et al., 2012), which label the meiotic axis and putative CO sites, respectively, and imaged using 3D-SIM microscopy. In total, we imaged 10 cells from 4 wild-type plants and 14 cells from 4 *zyp1a-2/zyp1b-1* plants, which provided sufficient data to quantitively compare with model simulations. By tracing along the linear SMC3 signals, using the SNT plugin to FIJI (Arshadi et al., 2021), we were able to segment the 10 axial elements in each cell (Figure 3A,B, top right panels). In

205 accordance with previous studies, we found that axial elements of homologous chromosomes were
206 tightly juxtaposed along their entire lengths in wild-type cells, whilst in the *zyp1a-2/zyp1b-1* line the
207 axes were only loosely paired along their lengths (Figure 3A,B, bottom rows), with the majority of
208 HEI10 foci being clearly located between the two homologous axes at an equivalent position along
209 their length (Figure 3A,B, right hand boxes) (Capilla-Pérez et al., 2021; France et al., 2021). Once the
210 paths of segmented axes had been extracted from the images, we were then able to use an
211 automated image analysis pipeline to assign HEI10 foci to specific positions along individual axes
212 based on their local proximity to those regions (Materials and Methods). Additionally, 3D-SIM
213 analysis of early pachytene cells in both the wild-type and *zyp1a-2/zyp1b-1* lines revealed a greater
214 number of less bright HEI10 foci than were observed in late-prophase I cells, which was consistent
215 with expectations (Figure 3 – figure supplement 1).

216 Nucleoplasmic coarsening model successfully predicts HEI10 foci patterning and intensities 217 in *zyp1* mutants

218 Using the experimental cytology and image analysis described above, we were able to construct
219 cytological late-HEI10 foci maps from both wild-type and *zyp1a-2/zyp1b-1* SC null mutant plants
220 (Figure 4A). In the wild-type we found an average of 9.0 late-HEI10 foci per cell, while in the *zyp1a-*
221 *2/zyp1b-1* line we found an average of 18.7 late-HEI10 foci per cell, which was broadly consistent
222 with previous cytological analyses of CO numbers in similar lines (Capilla-Pérez et al., 2021; France et
223 al., 2021).

224 When analysing the relative distribution of all late-HEI10 foci along chromosome pairs, we found
225 that in the *zyp1a-2/zyp1b-1* line the distribution of late-HEI10 foci was shifted towards more distal
226 positions, nearer the chromosome ends, when compared with the wild-type, which was also
227 consistent with previous genetic analysis of *zyp1* null mutants (Capilla-Pérez et al., 2021) (Figure 4A).
228 Importantly, nucleoplasmic coarsening model fits were capable of recapitulating this distribution,
229 with a preference for forming COs in more distal regions (Figure 4A). Such increases are a direct
230 consequence of the additional initial HEI10 loading applied to RIs near chromosome ends (Figure 1F),
231 which was a parameter that was included to improve the fit in the original coarsening model
232 (Morgan et al., 2021). Without the inclusion of this parameter, we would expect a flat distribution
233 with no preference for forming COs in more distal regions. Note that the extra loading here (up to
234 25% on the most distal 60% of each chromosome pair) is lower and more spread than that used in
235 the original model (up to 100% on the most distal 20%) (Figure 1 – figure supplement 1). The
236 increased end-loading of HEI10 was included in the original model because the dynamics of SC-
237 mediated coarsening naturally decrease the likelihood of RIs close to chromosome ends forming
238 COs. As there is an absence of SC-mediated-coarsening in the nucleoplasmic coarsening model, each
239 RI is equally capable of forming a CO regardless of its position. Thus, even though there is less
240 pronounced HEI10 end-loading in our nucleoplasmic coarsening model compared with our original
241 model (25% vs. 100%), this lower end-bias still causes a relative increase in distally positioned COs
242 under nucleoplasmic coarsening conditions compared with SC-mediated coarsening conditions. In
243 the original coarsening model, we hypothesised this end bias results from preferential synapsis near
244 the chromosome ends. In the absence of an SC there is obviously no synapsis, which explains why
245 the amount of end loading required within our nucleoplasmic-coarsening simulations is lower.
246 However, the preferential pairing of telomeres (to form the meiotic bouquet) (Varas et al., 2015),
247 which presumably still happens in the absence of an SC, may explain why a smaller end-bias for
248 HEI10 loading persists.

249 We also examined the spacing between adjacent late-HEI10 foci on the same chromosome pair. In
250 the wild-type, we found a scarcity of closely spaced crossovers, with a greater frequency of distantly
251 spaced COs, reflecting the action of CO interference (Figure 4B). This was consistent with our
252 previous analysis of wild-type CO patterning (albeit noisier due to the smaller sample size in this
253 study) (Morgan et al., 2021). In the *zyp1a-2/zyp1b-1* line, however, we found a very high frequency
254 of closely spaced crossovers, with a diminishing number of distantly spaced COs (Figure 4B). This
255 behaviour reflects an absence of CO interference, and provides strong cytological support for
256 previous conclusions drawn from genetic experiments in *zyp1* null mutants (Capilla-Pérez et al.,
257 2021). In this instance, the nucleoplasmic coarsening model was fully capable of predicting this
258 pattern of closely spaced COs, without additional parameterisation, validating the model and
259 reflecting an absence of CO interference (Figure 4B). Note, we use the term 'predicting' here and
260 below to define instances where the model simulations were capable of explaining data that was not
261 used to explicitly fit the model.

262 In addition to the late-HEI10 focus positioning data, we were also able to extract fluorescence
263 intensity measurements from each HEI10 focus in our imaging data. In wild-type *Arabidopsis,* we
264 previously showed that the normalized intensity of individual late HEI10 foci is negatively correlated
265 with the number of foci per bivalent, which is consistent with an SC-mediated-coarsening process
266 (Morgan et al., 2021). Here, we again identified such a correlation in wild-type plants (Figure 4C).
267 However, we did not find such a negative correlation in *zyp1a-2/zyp1b-1* mutants (Figure 4C). This
268 would be expected from a nucleoplasmic coarsening model as, in this scenario, HEI10 is equally
269 capable of diffusing through the nucleoplasm from any one RI to any other RI, regardless of whether
270 the other RI is located on the same chromosome pair or a different chromosome pair (see Figure
271 1A,B). Indeed, simulations of the nucleoplasmic coarsening model again predicted these findings
272 without the need for additional parameterisation and produced comparable results to the *zyp1a-*
273 *2/zyp1b-1* line (Figure 4C).

274 Combining synaptonemal complex- and nucleoplasm-mediated coarsening models

275 Although it appears likely that the SC acts as a conduit to promote HEI10 diffusion (Morgan et al.,
276 2021; Rog et al., 2017; Zhang et al., 2021, 2018), it remains unclear whether, in wild-type cells, the
277 SC is capable of irreversibly compartmentalising the diffusion of HEI10, such that there is little or no
278 recycling of SC-bound HEI10 back into the nucleoplasm. To address this question, we sought to
279 combine our original SC-mediated coarsening model, which assumes there is no recycling of SC-
280 bound HEI10 molecules back into the nucleoplasm (Morgan et al., 2021), with the nucleoplasmic
281 coarsening model (Methods, Figure 4 – figure supplement 1). We then tested whether this combined
282 model was still capable of robustly reproducing the experimental CO patterning results we
283 previously obtained from wild-type and HEI10 overexpressing *Arabidopsis* (Morgan et al., 2021)
284 (Figure 4 – figure supplement 2).

285 We used a combined version of the coarsening model, where the rates of absorption and escape
286 between the RI and the SC were set to be 90% of those in the original SC-mediated coarsening
287 model (Morgan et al., 2021), and the exchange rates between the RI and nucleoplasm were set to be
288 10% of those in the above nucleoplasmic coarsening model. We found that this combined model
289 was still fully capable of explaining the CO number and CO spacing distributions previously observed
290 in wild-type *Arabidopsis* (Figure 4 – figure supplement 2). Importantly, with this combined
291 coarsening ratio, we still observed only a very small proportion (<0.2%) of bivalents with zero COs
292 forming in our simulations and, hence, CO assurance is retained. This analysis demonstrates that a
293 scenario where the SC preferentially promotes retention and diffusion of HEI10 along the SC, but

294 without completely blocking HEI10 exchange between the SC and nucleoplasm, is still fully
295 compatible with the coarsening model for CO patterning. Additionally, by increasing total HEI10
296 concentration (both along the SC and at RIs) within our combined coarsening model simulations by
297 4.5-fold, we were able the reproduce CO number and CO spacing results previously obtained from
298 HEI10 over-expressor lines (Figure 4 – figure supplement 2).

299 The combined coarsening model explains CO patterning in mutants with partial synapsis

300 As well as investigating coarsening in wild-type plants, HEI10 over-expressors and in mutants that
301 completely lack an SC, we also sought to determine if the combined coarsening model could explain
302 CO patterning in mutants that exhibit partial, but incomplete, synapsis. In *Arabidopsis*, closely-
303 spaced crossovers have been observed in a number of mutants that exhibit partial synapsis, such as
304 *axr1*, *pss1* and *asy1* (Duroc et al., 2014; Jahns et al., 2014; Lambing et al., 2020; Pochon et al., 2022).
305 Intuitively, this common observation could be explained by the coarsening model. In the presence of
306 partial synapsis, the HEI10 protein would still preferentially load and diffuse along the SC, similar to
307 the wild-type situation. However, as the total length of SC available for HEI10 loading would be less
308 than wild-type, but the total nuclear concentration of HEI10 protein would presumably be the same
309 as wild-type, we anticipate that a higher concentration of HEI10 would be loaded per micron of SC
310 length. This situation is then similar to that found in a HEI10 over-expressor line, which has a greater
311 frequency of closely-spaced COs than wild-type, as previously explained by the coarsening model
312 (Morgan et al., 2021).

313 To test this theory, we investigated the patterning of late-HEI10 foci in an *Arabidopsis pch2* mutant.
314 PCH2 is a conserved AAA+ ATPase, with many known meiotic functions (Bhalla, 2022; Lambing et al.,
315 2015; Yang et al., 2022, 2020). In *Arabidopsis,* loss of PCH2 has been shown to compromise SC
316 polymerisation, generating a greater number of closely spaced COs, with no known effect on meiotic
317 DSB number (Lambing et al., 2015). Once again, we used 3D-SIM microscopy to assess and
318 quantitively evaluate the positions of HEI10 foci in late-pachytene *pch2-1* mutants (Figure 5A). In
319 total, we imaged 39 cells from 3 *pch2-1* plants. We found that late-HEI10 foci in *pch2-1* mutants
320 were exclusively associated with the short SC segments that form. On average, *pch2-1* cells
321 contained 14 (std. dev. ± 3) SC segments with an average length of 5.1 (std. dev. ± 4.4) µm. We
322 therefore mapped the position of HEI10 foci along these short SC segments using our bespoke image
323 analysis pipeline and quantified the number and position of late-HEI10 per SC segment within each
324 nucleus (Figure 5B-F, left hand plots). We detected 11.1 (σ^2 = 3.2) late-HEI10 foci per cell (Figure 5B),
325 with an average of 0.79 (σ^2 = 0.48) late-HEI10 foci per SC segment (Figure 5C). We also found that all
326 late-HEI10 foci were reasonably evenly distributed along SC segments (Figure 5D), and closely
327 spaced late-HEI10 foci were frequently detected (Figure 5E). Also, the longer SC segments tended to
328 have more late-HEI10 foci (Figure 5F), and the relative intensity of single late-HEI10 foci (i.e., foci on
329 SC segments that possess only a single focus) was positively correlated with SC segment length
330 (Figure 5G).

331 To determine if the combined coarsening model was capable of recapitulating the patterning effects
332 observed in *pch2-1* mutants, we ran simulations using the same number and length distribution of
333 SC segments per cell as in *pch2-1* mutants (Methods). This arrangement differed from wild-type
334 simulations where only five SC segments (corresponding to the five fully synapsed bivalents) were
335 simulated for each cell. Thus, each SC segment was effectively treated as a discrete bivalent within
336 our simulations (Figure 5 – figure supplement 1). As no HEI10 foci were detected outside SC
337 segments, no RIs were placed there, and these parts of the chromosomes were not included in our
338 simulations.

339 In *pch2-1* simulations, the total length of the SC per cell is shorter (roughly one-quarter in length)
340 than in wild-type, but the HEI10 amount is equivalent to that in wild-type simulations. This resulted
341 in an overall higher (roughly four times) concentration of HEI10 per µm of SC and at RIs. This is akin
342 to the situation in our HEI10 over-expressor simulations with SC-mediated coarsening (Morgan et al.,
343 2021). However, as with HEI10 over-expressor simulations, this ~4-fold increase in HEI10
344 concentration per µm of SC led to a smaller relative increase in the number of COs per unit length
345 because SC-mediated coarsening dynamics proceed more rapidly when the RIs with high levels of
346 HEI10 are closer together, as diffusion between them is easier. More rapid dynamics lead to
347 relatively fewer COs, as coarsening proceeds further in the same time period, with HEI10
348 accumulating in a smaller number of bright foci. We therefore reduced the rates of HEI10 exchange
349 between the RI and SC in order to slow the coarsening process, with an uptake rate of 20% and an
350 escape rate of 15% of the rates in the original SC-mediated coarsening model. Changes to SC
351 structure in the synaptic segments that occur in *pch2* mutants, versus wild-type SC, could account
352 for these modified exchange rates. These changes were combined with nucleoplasmic recycling at a
353 rate of 10% of that in the nucleoplasmic coarsening model. These simulations were then able to
354 qualitatively reproduce the patterning effects observed in our experimental data (Figure 5B-G, right
355 hand plots), although we note that agreement between experimental data and model outputs was
356 slightly less good for *pch2-1* than for the *zyp1* mutant. Specifically, using the *pch2-1* parameter
357 values we could generate an average of 11.0 (σ^2 = 5.2) COs per cell and 0.8 (σ^2 = 0.6) COs per SC
358 segment, which is similar to the mean and variance values in our imaging data (Figure 5B-C). We also
359 found that about 40% of simulated segments had no COs, which is similar to the proportion in our
360 experimental data. Additionally, we recapitulated the relatively flat distribution of COs within SC
361 segments (albeit with a slight peak in more central positions in simulation outputs that is not present
362 in the experimental data, Figure 5D), as well as reproducing the spacing between adjacent COs
363 (Figure 5E), and the positive correlations between both CO number (Figure 5F) and single late-HEI10
364 focus relative intensity (Figure 5G) and SC length.

365 Discussion

366 It was recently shown that the synaptonemal complex (SC), a highly conserved and prominent
367 feature of meiotic prophase I, is required to promote CO interference and CO assurance in
368 *Arabidopsis thaliana* (Capilla-Pérez et al., 2021; France et al., 2021). However, the mechanistic
369 details of precisely how the SC plays a role in mediating interference remained obscure. Here, using
370 a combination of modelling and super-resolution microscopy, we have shown that CO patterning in
371 the absence of an SC is consistent with a coarsening model for CO interference. Previously, we
372 introduced a mechanistic, mathematical coarsening model that could explain CO patterning in wild-
373 type *Arabidopsis*, as well as in HEI10 over and under-expressor lines (Morgan et al., 2021). Here, we
374 make just one major change to the model for SC mutants: that HEI10 can now exchange through a
375 nucleoplasmic pool rather than being restricted to individual chromosomes, as in the wild-type. With
376 this biologically plausible modification, the coarsening model is now also capable of explaining why
377 *zyp1* mutants lack CO assurance and CO interference in *Arabidopsis*. Additionally, the model
378 successfully predicts previously unexplored observations in *zyp1* SC mutants, including the pattern of
379 closely-spaced COs and the absence of an anticorrelation between HEI10 focal intensity and focus
380 number per chromosome pair. A similar function of the SC, in preventing the diffusion of
381 recombination proteins via the nucleoplasm, has been proposed in *C. elegans* (Rog et al., 2017;
382 Zhang et al., 2021, 2018). However, unlike in *C. elegans* where successful CO formation depends
383 upon SC formation (Colaiácovo et al., 2003), in *Arabidopsis* SC formation and CO formation can be
384 uncoupled (Capilla-Pérez et al., 2021; France et al., 2021), making *Arabidopsis* an excellent system

385 for demonstrating the effects of nucleoplasmic coarsening. Overall, our work highlights the critical
386 role of the SC in controlling the spatial compartment through which HEI10 diffuses.

387 Recently, a study in *Arabidopsis* also successfully utilised the mathematical coarsening model
388 (originally derived in Morgan et al., 2021) to explain genetic CO patterning data from wild-type and
389 HEI10 overexpressing *Arabidopsis* (Durand et al., 2022). The authors also hypothesised that
390 nucleoplasmic coarsening could explain CO patterning in *zyp1* mutants, and in *zyp1* mutant and
391 HEI10 overexpressing lines that form extremely high numbers of COs. However, unlike in this work,
392 the dynamics of nucleoplasmic coarsening were not explicitly modelled (Durand et al., 2022).

393 Interestingly, while *Arabidopsis zyp1* mutants lose CO interference, they still display a non-random
394 (sub-Poissonian) distribution of COs per cell. In wild-type cells, CO interference operating along
395 individual chromosomes regulates total CO numbers along each chromosome. In turn, the combined
396 effect of interference operating along all chromosome pairs within a cell causes global regulation of
397 the total number of COs within a cell, with the variance in total CO number per cell being close to
398 the sum of the per chromosome variances. In some species, COs have been shown to co-vary,
399 meaning a high CO number on one chromosome generally corresponds with high CO numbers on
400 other chromosomes within the same cell. This leads to a broader distribution of CO numbers per cell
401 than might be expected (Wang et al., 2019). However, recent results suggest that CO co-variation is
402 not present in *Arabidopsis* (Durand et al., 2022). *zyp1* mutants lose CO interference but retain per-
403 cell constraints on total CO numbers, as evidenced by the Poissonian and sub-Poissonian
404 distributions of total CO numbers on individual chromosome pairs and in individual cells,
405 respectively. In other words, in the *zyp1* mutant, COs designated on different RIs are spatially
406 independent from one another but their numbers are not independent. As noted in (Crismani et al.,
407 2021), an explanation for why CO numbers are relatively low (but still higher that wild-type) in SC
408 mutants could be due to the influence of a limiting trans-acting factor, such as HEI10. Similarly, in
409 our modified coarsening model, the limited nucleoplasmic pool of HEI10 explains why the
410 distribution of total CO numbers per cell remains sub-Poissonian. Importantly, caution should be
411 exercised when interpreting sub-Poissonian or Poissonian distributions of total CO number per cell
412 as signs of functional or non-functional CO interference, respectively. As we show here, a sub-
413 Poissonian distribution is perfectly compatible with non-functional CO interference.

414 Importantly, as well as explaining CO patterning in mutants without synapsis, we have shown that a
415 version of the coarsening model that incorporates both nucleoplasmic and SC-mediated coarsening
416 is still fully capable of explaining CO patterning in wild-type and HEI10 overexpressing *Arabidopsis.*
417 This builds on a previous version of the coarsening model, where HEI10 diffusion was restricted
418 exclusively to the SC (Morgan et al., 2021). We anticipate that this new, combined coarsening model
419 likely better reflects the biological reality of the coarsening process, with the SC promoting and
420 enhancing the diffusion of HEI10 along individual bivalents but with some exchange of HEI10
421 molecules between the SC and the nucleoplasm. This leakage is incorporated here as exchange
422 between RIs and the nucleoplasm, but it is straightforward to also include direct exchange between
423 the SC and the nucleoplasm in the framework of this model.

424 The complex interplay between SC-mediated and nucleoplasmic coarsening can also provide a
425 potential mechanistic explanation for other crossover phenomena, such as the interchromosomal
426 effect (Miller, 2020; Termolino et al., 2019).The interchromosomal effect describes the observation
427 that when one pair of homologs experiences a reduction in crossover frequency (due to a structural
428 variation, such as an inversion) this is accompanied by a corresponding increase in crossover
429 frequency on the other, structurally normal, homolog pairs (Miller, 2020; Termolino et al., 2019). In
430 this scenario, RIs may be inhibited from occurring normally at the sites of structural variations,

leading to a lower level of HEI10 in those regions. In turn, this could lead to a redistribution of the limited pool of HEI10 to the other chromosomes, thus increasing the likelihood of those chromosomes receiving extra COs.

Additionally, we have shown that HEI10-coarsening can explain aspects of CO patterning in *pch2* mutants that exhibit partial, but incomplete, synapsis (Lambing et al., 2015). In this scenario, available HEI10 molecules could still load onto the SC and undergo coarsening, similar to the situation in the wild-type. However, if a wild-type level of HEI10 protein is loaded onto shorter stretches of SC, this results in an increased concentration of HEI10 per micron of SC and, akin to the situation in an otherwise wild-type HEI10 over-expressor (Morgan et al., 2021), an increase in closely-spaced COs within those stretches. An abundance of closely spaced COs have also been reported in other *Arabidopsis* mutants that exhibit partial synapsis, such as *axr1*, *pss1* and *asy1* (Duroc et al., 2014; Jahns et al., 2014; Lambing et al., 2020; Pochon et al., 2022), suggesting that the coarsening model could explain CO patterning in a variety of synaptic mutants.

Together, the results we present here further reinforce the ability of the coarsening paradigm to explain numerous aspects of CO control in both wild-type and mutant *Arabidopsis* lines. These aspects include: CO placement, CO frequency, CO assurance, CO interference, CO homeostasis, heterochiasmy, meiotic duration, interchromosomal effects and diverse HEI10 focal intensity measurements. Given the conserved nature of HEI10 (Agarwal and Roeder, 2000; Chelysheva et al., 2012; Jantsch et al., 2004; Lake et al., 2015; Qiao et al., 2014; Reynolds et al., 2013), and the discovery of similar coarsening mechanisms in *C. elegans* (Zhang et al., 2021), it is likely that similar mechanisms regulate these same crossover patterning phenomena in a wide variety of sexually reproducing eukaryotes.

Acknowledgments

We gratefully acknowledge James Higgins for providing the *zyp1a-2/zyp1b-1* mutant seeds, Chris Franklin for supplying the SMC3, HEI10 and ZYP1 antibodies, Eva Wegel for microscopy support and members of the M. Howard and X. Feng labs for fruitful discussions on this topic. This work was supported by a BBSRC Discovery Fellowship (BB/V005774/1) awarded to C.M. and by BBSRC Institute Strategic Programme GEN (BB/P013511/1) to M.H.

Materials and methods

Key Resources Table

Key Resources Table				
Reagent type (species) or resource	**Designation**	**Source or reference**	**Identifiers**	**Additional information**
gene (*Arabidopsis*)	ZYP1A	TAIR	AT1G22260	
gene (*Arabidopsis*)	ZYP1B	TAIR	AT1G22275	

gene (*Arabidopsis*)	PCH2	TAIR	AT4G24710	
strain, strain background (*Arabidopsis*)	*zyp1a-2/zyp1b-1*	France *et al.,* 2021		Supplied by Dr James Higgins, University of Leicester
strain, strain background (*Arabidopsis*)	*pch2-1*	Syngenta Arabidopsis Insertion Library (SAIL)	SAIL_1187_C06	
antibody	anti-HEI10 (rabbit polyclonal)	Lambing et al., 2015		Supplied by Prof Chris Franklin, University of Birmingham (1:500 dilution)
antibody	anti-SMC3 (rat polyclonal)	Ferdous et al., 2012		Supplied by Prof Chris Franklin, University of Birmingham (1:500 dilution)
antibody	anti-ZYP1 (guinea-pig polyclonal)	France et al., 2021		Supplied by Prof Chris Franklin, University of Birmingham (1:500 dilution)
antibody	alexa fluor 555 goat anti-rabbit (goat polyclonal)	Thermo Fisher	RRID AB_2535849	(1:200 dilution)
antibody	alexa fluor plus 488 goat anti-rat (goat polyclonal)	Thermo Fisher	RRID AB_2896330	(1:200 dilution)
antibody	alexa fluor 647 goat anti-guinea-pig (goat polyclonal)	Thermo Fisher	RRID AB_2735091	(1:200 dilution)
sequence-based reagent	PCH2_1_FV	Lambing et al., 2015	PCR primers	CAGTGCAAATAGCCGTCGCTGAG
sequence-based reagent	PCH2_1_RV	Lambing et al., 2015	PCR primers	CTCACATGGTCCTTCTTCAATGAGC
sequence-based reagent	Sail LB2	Lambing et al., 2015	PCR primers	GCTTCCTATTATATCTTCCCAAATTACCAATACA
sequence-based reagent	zyp1_ns_1	France et al., 2021	PCR primers	CTCGCATTTGCTGGTTTAAAGAGTC
sequence-based reagent	zyp1b_sp_1	France et al., 2021	PCR primers	TGCGTATATTGCTAGGTTTATATTG

sequence-based reagent	salk_lb2	France et al., 2021	PCR primers	GTGCTTTACGGCACCTCGAC
sequence-based reagent	zyp1a_sp_1	France et al., 2021	PCR primers	GAATAGTTAGCAGATTCATATTTCAC
peptide, recombinant protein	HindIII-HF	NEB	R3104S	
chemical compound, drug	cytohelicase	Sigma-Aldrich	C8274	
chemical compound, drug	polyvinylpyrrolidone	Sigma-Aldrich	PVP40	
software, algorithm	FIJI	Schindelin et al. 2012	2.1.0/1.53f51	
software, algorithm	Zen Black	Zeiss	14.0.12.201	
software, algorithm	Python	Python	RRID:SCR_008394	https://www.python.org/
software, algorithm	R	R Project for Statistical Computing	RRID:SCR_001905	http://www.r-project.org/
software, algorithm	Julia	Julia	RRID:SCR_021666	https://julialang.org/

Plant Materials

Arabidopsis thaliana lines used in this study were wild-type Col-0, *pch2-1* (SAIL_1187_C06) and the *zyp1a-2/zyp1b-1* null-mutant (previously characterised in (France et al., 2021)). The *zyp1a-2/zyp1b-1* line contains a CRISPR/Cas9 derived 14 base-pair deletion in exon 3 of *ZYP1A* and a T-DNA insertion in exon 3 of *ZYP1B.* Plants were grown in controlled environment rooms with 16 h of light (125 mMol cool white) at 20 °C and 8 h of darkness at 16 °C.

Immunocytology

Immunocytology of spread *Arabidopsis thaliana* pachytene cells was performed as described previously (Morgan et al., 2021; Morgan and Wegel, 2020). In brief, staged anthers were dissected from *Arabidopsis* floral buds and macerated in a 10 µl drop of digestion medium (0.4% cytohelicase, 1.5% sucrose, 1% polyvinylpyrolidone in sterile water) on a No. 1.5H coverslip (Marienfeld). Coverslips were then incubated in a moist chamber at 37 °C for 4 minutes before adding 10 µl of 2% lipsol solution followed by 20 µl of 4% paraformaldehyde (pH 8). Coverslips were dried for 3 hours in the fumehood and then blocked in blocking buffer (0.3% BSA in 1 x PBS) for 15 minutes. 50 µl of primary antibody, diluted in blocking buffer, was added to the coverslips and they were then

477 incubated overnight in a moist chamber at 4 °C. 50 µl of secondary antibody, diluted in blocking
478 buffer, was added to the coverslips and they were then incubated in a moist chamber at 37 °C for 2
479 hours. Coverslips were then incubated in 10 µl DAPI (10 µg/ml) for 5 min before adding 7 µl of
480 Vectashield and mounting them on a glass slide. Coverslips were washed for 3 x 5 minutes in 1 X PBS
481 0.1% Triton before and after each incubation step. The following primary antibodies were used at
482 1:500 dilutions: anti-SMC3 (rat) (Ferdous et al., 2012), anti-HEI10 (rabbit) (Lambing et al., 2015) and
483 anti-ZYP1 (guinea-pig) (France et al., 2021). The following secondary antibodies were used at 1:200
484 dilutions: anti-rat Alexa Fluor Plus 488 (ThermoFisher A48262), anti-rabbit Alexa Fluor 555
485 (ThermoFisher A21428) and anti-guinea-pig Alexa Fluor 647 (ThermoFisher A21450). Immunostained
486 cells were imaged using 3D structured illumination microscopy (3D-SIM) on a Zeiss Elyra PS1
487 microscope equipped with an EM-CCD camera, a Plan-Apochromat ×63, NA 1.40 oil objective and
488 405, 488, 561 and 642 nm solid-state laser diodes. Cells were imaged with three stripe angles and
489 five phases and z-stacks were captured at an interval size of 0.0909 µm. An immersion oil with a
490 refractive index of 1.515 was used that was optimised for the green/red (SMC3/HEI10) channels of
491 our system. For optimal image quality and to minimise the introduction of reconstruction artefacts,
492 microscope laser power and camera gain values were manually adjusted for each cell. Bleaching and
493 contrast of raw images was assessed using the SIMcheck plugin to FIJI (Ball et al., 2015).

494 ## Image analysis

495 For wild-type and *zyp1a-2/zyp1b-1* nuclei, individual axes were traced and segmented in 3-
496 dimensions from 3D-SIM z-stacks using the SNT plugin to FIJI (Arshadi et al., 2021). Traces were
497 made using the linear SMC3 signal, which localises along the meiotic axis, and 3D-skeletons of each
498 axis-traced path were generated using SNT. For *zyp1a-2/zyp1b-1* nuclei, each axial element was
499 traced end-to-end to generate 10 complete skeleton traces for each nucleus. For wild-type nuclei,
500 due to the proximity of the two parallel SMC3 signals, a single trace was used to segment the paths
501 of each pair of synapsed axial elements, generating 5 complete skeleton traces for each nucleus. Foci
502 were detected within images using the FociPicker3D Fiji plugin (Du et al., 2011). Uniform background
503 intensity thresholds and minimum pixel size values were manually optimised within a range of
504 6,000-20,000 and 5-20, respectively, with otherwise default parameters. Further analysis was
505 performed using custom Python scripts. For *zyp1a-2/zyp1b-1* nuclei, foci were assigned to the
506 chromosome pair for which the average of the two distances from the closest points on each of the
507 axes was smallest, provided this was less than a threshold distance (0.5 µm). If this was not the case,
508 then the foci was assigned to the closest chromosome pair, provided that it was nearer to one of the
509 two axes than a smaller threshold (0.3 µm). Foci satisfying neither of these two criterion were
510 considered as off target signal and ignored. For wild-type nuclei, each focus was assigned to the
511 closest trace, provided that it was nearer than a threshold (0.5 µm). Again, foci not satisfying this
512 criterion were considered as off target signal and ignored. Relative positions along chromosome
513 pairs were calculated by dividing the distance along the traced axis (measured in terms of voxels) by
514 the total length of the trace. Foci intensities were calculated using the mean intensity within a
515 sphere of radius 0.1985 µm (5 voxels in the x and y planes), centred at the foci peak, and the median
516 intensity of the image (used as an estimate of the background fluorescence) was subtracted. All
517 intensity values used were normalized by dividing the foci intensity by the mean of the intensities of
518 all foci within the same cell (only considering foci associated with a chromosome pair). Simple linear
519 regression was performed using the Python statsmodels package.
520
521 For *pch2-1* nuclei, segments of synapsis were traced and segmented in 3-dimensions from 3D-SIM z-
522 stacks using the SNT plugin to FIJI (Arshadi et al., 2021). Traces were made using the linear ZYP1
523 signal, which localises along the SC, and 3D-skeletons of each SC-traced path were generated using

SNT. Each SC segment was traced end-to-end to generate between 8 and 21 complete skeleton traces for each nucleus. Individual traces varied from 0.4 to 28.4 µm in length. Again, foci were detected within images using the FociPicker3D Fiji plugin (Du et al., 2011). Uniform background intensity thresholds and minimum pixel size values were manually optimised within a range of 10,000-15,000 and 10-20, respectively, with otherwise default parameters. Further analysis was performed using custom Python scripts. All subsequent analysis proceeded as for wild-type nuclei.

Mathematical models

Nucleoplasmic coarsening model

In each cell, $Q = 5$ chromosome pairs are simulated. The q-th chromosome pair is taken to have a length L_q, sampled from the (per-chromosome) normal distribution $\mathcal{N}_T(\mu_q, \sigma_q^2, -3,3)$ truncated at 3 standard deviations from the mean (to ensure positive chromosome lengths). We use the same values as in our earlier work (Morgan et al., 2021), fitted to experimentally measured wild-type chromosome length distributions: $\mu_1 = 37.5, \mu_2 = 40.4, \mu_3 = 45.7, \mu_4 = 53.8, \mu_5 = 59.8$, and $\sigma_1 = 4.93, \sigma_2 = 5.06, \sigma_3 = 5.86, \sigma_4 = 7.18, \sigma_5 = 7.13$, with all these parameters having units of μm. We chose to retain these original values as they were broadly consistent with the experimental chromosome lengths measured in this study, but were calculated from a greater sample size.

Recombination intermediates (RIs) are placed randomly along each of the chromosome pairs, with a probability density ρ per µm. To implement this, for each simulated chromosome pair with length L, a random number is generated from a Poisson process with mean ρL, and then this number of RIs are placed uniformly at random along that chromosome pair. We note that this procedure differs slightly from the method used in our original SC coarsening model, where floor(ρL) crossovers were placed on a chromosome with length L. Simulation outputs with this original rule (not shown) differ only slightly.

The pro-crossover factor HEI10 is present in a nucleoplasmic pool, with amount P, and at compartments at each of the RIs, with amounts $C_{q,n}$, $1 \leq q \leq \mathrm{Q} = 5$, $1 \leq n \leq N_q$ for n-th RI on the q-th chromosome pair. HEI10 is able to move between the nucleoplasmic pool to each of the RI compartments at rate α, and to escape from the RI compartments back into the pool at a rate $\beta(C_{q,n})$, which depends on the amount of HEI10 within each individual RI compartment. Figure 1D shows the functional form of this rate in more detail, from which we see that it is a strictly decreasing function of the RI HEI10 amount $C_{q,n}$. As in our SC interference model, we take

$$\beta(C_{q,n}) = \frac{\beta_C}{1 + (C_{q,n}/K_C)^{\gamma}}.$$

The system of ordinary differential equations governing HEI10 amounts is

$$\frac{\mathrm{d}C_{q,n}}{\mathrm{d}t} = (\alpha P - \beta(C_{q,n})C_{q,n})H_s(C_{q,n} - K_H), \qquad 1 \leq q \leq Q,\ 1 \leq n \leq N_q,$$

$$\frac{\mathrm{d}P}{\mathrm{d}t} = \sum_{q=1}^{Q}\sum_{n=1}^{N_q} H_s(C_{q,n} - K_H)(\beta(C_{q,n})C_{q,n} - \alpha P).$$

Compared to our earlier model (Morgan et al., 2021), we also incorporated a further modulation to the HEI10 exchange rates between the nucleoplasm and RIs, through the multiplicative smoothing function H_s. For HEI10 levels in an RI well below a threshold K_H, the smoothing function becomes close to zero, while for levels well above, the function saturates to one, with a smooth crossover in

between. This feature ensures that RIs with HE10 levels well below the threshold become disconnected, with their HEI10 effectively disappearing from the rest of the system. This reflects the experimental observation that smaller HEI10 foci are not detected in late-pachytene nuclei (Morgan et al., 2021), with RIs that lack sufficient HEI10 presumably being channelled into a non-crossover or class II repair pathway. We implement this through the smooth cutoff function H_s :

$$H_s(s) = \frac{1}{2}\big(1 + \tanh(K_s s)\big)$$

which multiplies the HEI10 exchange rates between the RIs and nucleoplasm. Overall, this system conserves the total amount of HEI10 within each cell (the nucleoplasmic pool plus all RI compartments), rather than within each SC, which was the case for our earlier SC-mediated coarsening model (Morgan et al., 2021).

Unlike in our previous SC-mediated coarsening model, where the total HEI10 amount in each cell depended on the total length of SC and the total number of RIs (which are relatively constant from cell to cell), we adopted an alternative approach for controlling cellular HEI10 amount in our simulations. This change was necessary due to the absence of an SC in the nucleoplasmic-coarsening model, and is likely more realistic, with cellular HEI10 protein amount being controlled independently of SC formation, as we now describe.

The initial total amount of HEI10 within each cell, F, is sampled from a truncated normal distribution

$$F = \mathcal{N}_T(\mu_F, \sigma_F^2, -3{,}3),$$

where the mean μ_F and standard deviation σ_F are taken to be the mean and standard deviation of the total amounts of HEI10 within each cell in the original SC-mediated coarsening model (Morgan et al., 2021). This initial cellular level of HEI10 is divided between the RIs and the nucleoplasmic pool, at constant proportions R_{RI} and R_P, respectively, with $R_{RI} + R_P = 1$.

The total amount of RI HEI10 is then randomly divided between each RI, where, for each RI, a random weighting $\hat{C}_{q,n}$ is generated from

$$\hat{C}_{q,n} = f\left(\frac{x_{q,n}}{L_q}\right) X_{q,n}, \qquad X_{q,n} = \mathcal{N}_T(1, \sigma_C^2, -3{,}3), \qquad 1 \le q \le Q,\ 1 \le n \le N_q,$$

where $\mathcal{N}_T$ again denotes a truncated normal distribution and $x_{q,n}$ is the position of the n-th RI on the q-th chromosome pair. The piecewise function $f(x/L)$, included to account for the increased frequency of crossovers towards the end of each chromosome, is defined as

$$f(\xi) = \begin{cases} 1 + (f_e - 1)(1 - \xi/x_e) & 0 \le \xi \le x_e, \\ 1 & x_e \le \xi \le 1 - x_e, \\ 1 + (f_e - 1)(\xi - 1 + x_e)/x_e & 1 - x_e \le \xi \le 1. \end{cases}$$

The total initial amount of HEI10 at all RIs, $R_{RI}F$, is then loaded at the RIs in proportion to these weights, namely

$$C_{q,n}(t = 0) = R_{RI} F \frac{\hat{C}_{q,n}}{\sum_{q'=1}^{Q} \sum_{n'=1}^{N_q} \hat{C}_{q',n'}}.$$

The remaining HEI10 is placed in the nucleoplasmic pool, with initial amount $P(t=0)=R_P F$, which has the same average as the average amount of HEI10 loaded onto all the SCs in the original SC-mediated coarsening model (Morgan et al., 2021).

This system is simulated for a duration $T=10$hr, a duration of pachytene equivalent to that used in our original model (Prusicki et al., 2019). Numerical simulations are performed using the Rodas5 solver (di Marzo, 1992) of the DifferentialEquations.jl Julia package (Rackauckas and Nie, 2017), with a non-negativity constraint on HEI10 amounts. The initial conditions for the simulation are random, but the evolution of the system is deterministic. Multiple simulations (10000) with different random initial conditions are performed to determine the distribution of crossover numbers, positions and intensities. At the end of each simulation, RIs are designated as crossover sites according to a modified rule (see "Modified CO criterion" below).

All parameters were chosen to be the same as those as in the original SC coarsening model (Morgan et al., 2021), except for the RI HEI10 absorption rate α, and the (maximum) escape rate β_C, which was multiplied by a factor of 0.06 (Figure 1E). These changes reflect that HEI10 is now being exchanged with the nucleoplasmic pool, rather than locally on the synaptonemal complex.

For simulations of the *zyp1* HEI10 over-expressor line, a 3.5-fold change in HEI10 levels was used, but a larger fold change was chosen for the standard deviation σ_F of total cellular HEI10 amounts, in order to generate greater cell-cell variability, with an increase from 75 a.u. to 860 a.u. We also verified that increasing the noise to this degree in the original model of (Morgan et al., 2021) (as implemented below) for wild-type and HEI10 overexpressing lines, did not make a substantial difference to model predictions for the number of COs per SC, or the positioning of COs. We note that the above 3.5-fold change in HEI10 levels resulted in roughly the same relative change in CO number, unlike for SC-mediated coarsening where 4.5 times the level of HEI10 only resulted in approximate doubling of the number of COs (Morgan et al., 2021). This reduced change reflects the reduced sensitivity of the SC-mediated coarsening to changes in HEI10 levels, compared to nucleoplasmic-mediated coarsening (for these choices of parameter values).

SC-mediated coarsening model

This model is as described in our earlier work, but with the introduction of the smooth cutoff function preventing recycling at RIs with low levels of HEI10, with slightly different initial conditions, and with a new rule for determining which RIs are crossovers at the end of the simulation. Again, $Q=5$ chromosomes are simulated in each cell, these having SCs with lengths L_q generated randomly as in the nucleoplasmic coarsening model. HEI10 is present on each of the SCs with concentration $c_q(x,t)$ per unit length, and is able to diffuse along them with (one-dimensional) diffusion coefficient D. RI numbers and positions are generated as in the nucleoplasmic model. Again, we note that this is slightly different to the rule used in (Morgan et al., 2021), but that this change has limited effect on model outputs. The variables $C_{q,n}$ represent the amount of HEI10 associated with the n-th RI on the q-th SC. However, RIs are not able to exchange HEI10 with the nucleoplasm, but instead exchange HEI10 with the relevant SC, with uptake rate $\hat{\alpha}$ and escape rate $\hat{\beta}(C_{q,n})$, this escape rate taking the same functional form as in the nucleoplasmic coarsening model but with the new parameter $\hat{\beta}_C$. This gives the system of equations

$$\frac{\mathrm{d}C_{q,n}}{\mathrm{d}t} = \left(\hat{\alpha} c_q(x_{q,n}) - \hat{\beta}(C_{q,n}) C_{q,n}\right) H_s(C_{q,n} - K_H), \qquad 1 \le q \le Q,\ 1 \le n \le N_q,$$

$$\frac{\partial c_q}{\partial t} = D\frac{\partial^2 c_q}{\partial x^2} + \sum_{n=1}^{N_q}\left(\hat{\beta}(C_{q,n})C_{q,n} - \hat{\alpha}c_q\left(x_{q,n}\right)\right)H_s(C_{q,n} - K_H)\delta(x - x_{q,n}),$$

$$1 \le q \le Q,\ 0 \le x \le L_q,$$

$$\frac{\partial c_q}{\partial x} = 0, \text{ at } x = 0 \text{ and } x = L_q,$$

$$c_q = c_0 \text{ at } t = 0.$$

Initial conditions for total cellular HEI10 levels are as in the nucleoplasmic model. Initial RI HEI10 amounts are as in the nucleoplasmic model, but with different parameters (see Figure 4 – supplementary figure 1) in the non-uniform loading function $f(\xi)$. However, instead of being placed in the nucleoplasmic pool, the remaining HEI10 is placed uniformly on the SCs, giving

$$c_q(t = 0) = c_0 = \frac{R_{SC}F}{\sum_{q'=1}^{Q} L_{q'}},$$

where $R_{SC} = 1 - R_{RI}$. Note that these initial conditions differ from those used in (Morgan et al., 2021), but when the new rule for determining crossovers is used, they give very similar results in terms of crossover number and location. This model was used to produce the simulation output shown in Figure 4 – figure supplement 2 (WT, OX), using the parameters shown in Figure 4 - figure supplement 1D (WT column), except for the over-expressor OX case, where the parameters μ_F and σ_F controlling initial cellular HEI10 levels were increased to 4.5x their WT values.

Combined coarsening model

The combined model includes all the above rules in the nucleoplasmic and SC-mediated coarsening models, with HEI10 being present in RI, SC and nucleoplasm compartments. The governing equations are a combination of those in the two other models; explicitly,

$$\frac{\mathrm{d}C_{q,n}}{\mathrm{d}t} = \left(\alpha P - \beta(C_{q,n})C_{q,n} + \hat{\alpha}c_q\left(x_{q,n}\right) - \hat{\beta}(C_{q,n})C_{q,n}\right)H_s(C_{q,n} - K_H),$$

$$1 \le q \le Q,\ 1 \le n \le N_q,$$

$$\frac{\partial c_q}{\partial t} = D\frac{\partial^2 c_q}{\partial x^2} + \sum_{n=1}^{N_q}\left(\hat{\beta}(C_{q,n})C_{q,n} - \hat{\alpha}c_q\left(x_{q,n}\right)\right)H_s(C_{q,n} - K_H)\delta(x - x_{q,n}),$$

$$1 \le q \le Q,\ 0 \le x \le L_q,$$

$$\frac{\mathrm{d}P}{\mathrm{d}t} = \sum_{q=1}^{Q}\sum_{n=1}^{N_q}\left(\beta(C_{q,n})C_{q,n} - \alpha P\right)H_s(C_{q,n} - K_H).$$

Initial and boundary conditions for wild-type or HEI10 over-expressor plants are as in the SC-mediated coarsening model above. No HEI10 is placed initially in the nucleoplasm. Each SC is discretized into m=2000 compartments, and the spatial derivatives approximated by finite differences. This model was used to generate the simulation output shown in Figure 4 – figure supplement 2 (WT+nuc, OX+nuc), using the parameters shown in Figure 4 - figure supplement 1D (WT+nuc column), except for the over-expressor OX+nuc case, where the parameters μ_F and σ_F controlling initial cellular HEI10 levels were increased to 4.5x their WT values.

For the *pch2-1* mutant, we have a variable number of SC segments within the cell, which are here treated as distinct SCs. The number of SC segments is drawn randomly from a Poisson distribution with mean 13.92 (close to that measured experimentally), while the length of each SC segment is drawn from a Gamma distribution with parameters $L_\alpha = 1.693$, $L_\theta = 2.984\ \mu\text{m}$, so having mean $L_\alpha L_\theta \approx 5.1\mu\text{m}$ and variance $L_\alpha L_\theta^2 \approx 15.1\mu\text{m}^2$. This distribution has probability distribution function

$$f_\Gamma(x; L_\alpha, L_\theta) = \frac{x^{L_\alpha - 1} e^{-x/L_\theta}}{\Gamma(L_\alpha) L_\theta^{L_\alpha}}, \quad x > 0,$$

where $\Gamma(x)$ is the Gamma function, and was fitted to experimental measurements of SC segment length. This statistical model for SC segment lengths introduced substantially greater variation in total cellular SC length than in the other simulations, which motivated our new rule for the assignment of initial HEI10 amounts. Initial and boundary conditions are the same here as for the SC-mediated coarsening model above (although there are a larger number of SCs here).

Owing to this large number of SCs, all of which are coupled with each other through the nucleoplasm, for efficient simulation each SC segment is spatially discretized into $m = 200$ portions, fewer than the number ($m = 2000$) used for each SC in the SC-mediated coarsening model above.

The smooth cutoff function H_s is included so that RIs with low levels of HEI10 are unable to interact with the nucleoplasmic pool. This is necessary, as otherwise these RIs provide an additional route for the transfer of HEI10 between two RIs on the same SC: HEI10 can diffuse along the SC from a RI losing HEI10 to a nearby RI with low levels of HEI10, escape into the nucleoplasm, be reabsorbed at another RI with low levels of HE10, and then diffuse along the SC to an RI gaining HEI10. This route causes the dynamics to progress too quickly.

The parameterization of this combined model used for the *pch2-1* mutant has substantially smaller values for the rates of exchange of HEI10 between RIs and SCs ($\hat{\alpha}$ and $\hat{\beta}_C$) than in the original SC-mediated coarsening model (Figure 5 – Figure supplement 1C). These were chosen to better fit the experimental data, which shows a less pronounced spatial pattern than the wild-type data. Nucleoplasmic recycling was also set at a rate of 10% of that in the nucleoplasmic coarsening model. This model was used to generate the simulation output shown in Figure 5.

SC-mediated coarsening model analysis

In the SC-mediated coarsening model, as the timescale for diffusion along the SC ($\sim L^2/D$, which is at most $(60\mu\text{m})^2/1.1\mu\text{m}^2\text{s}^{-1} \approx 3300\text{s}$) is small compared with the duration of pachytene (36000s), the HEI10 concentration adopts a piecewise linear profile along each SC, with discontinuities in its slope at each RI. When there are just two RIs with HEI10 amounts C_1 and C_2, separated by a distance $\Delta x = x_2 - x_1$, we have that

$$\frac{dC_1}{dt} = \hat{\alpha} c(x_1) - \hat{\beta}(C_1) C_1 = -J, \quad \frac{dC_2}{dt} = \hat{\alpha} c(x_2) - \hat{\beta}(C_2) C_2 = J,$$

where the net flux of HEI10 from C_1 to C_2, J, is given by

$$J = D \frac{c(x_1) - c(x_2)}{\Delta x}.$$

On eliminating $c(x_1)$ and $c(x_2)$, the concentrations of HEI10 on the SC at the two RIs, we find that

$$\frac{d}{dt}(C_2 - C_1) = \frac{\hat{\beta}(C_1) C_1 - \hat{\beta}(C_2) C_2}{1 + \frac{\hat{\alpha}\Delta x}{2D}}.$$

We can see from this equation that closely spaced pairs of RIs, with small Δx, coarsen more quickly than those further apart. This effect generates spatial patterns in CO positioning, even in the absence of non-uniform initial HEI10 loading. However, this difference in coarsening rate is only significant if $\frac{\hat{\alpha}\Delta x}{2D}$ is not small compared with 1. In the limit where $\frac{\hat{\alpha}\Delta x}{2D}$ is small, the spatial patterns in CO positioning vanish, other than those spatial biases from non-uniform initial HEI10 loading.

With $K_C = 1$ and for $C_1, C_2 \gg 1$ and $\frac{\hat{\alpha}\Delta x}{2D} \gg 1$, which is the case for our original SC-mediated coarsening parameters, this can be approximated further as

$$\frac{d}{dt}(C_2 - C_1) = \frac{2\,D\,\hat{\beta}_C}{\hat{\alpha}\Delta x}\left(C_1^{1-\gamma} - C_2^{1-\gamma}\right).$$

From this equation, we find that coarsening proceeds faster for larger diffusion coefficients, larger escape rates from RIs to the SC, and slower for larger uptake rates from the SC to RIs, more widely spaced RIs, and when HEI10 levels are greater (as $\gamma > 1$). When more than two RIs are participating in coarsening, a more complex system of equations is obtained, but again containing the model parameters in the same combination $\frac{D\,\hat{\beta}_C}{\hat{\alpha}}$. As a consequence of this, it is difficult from simulation outputs to independently identify the parameters $\hat{\alpha}$, $\hat{\beta}_C$ and D, with many parameter sets being potentially compatible with our original findings.

Modified crossover criterion

In our original simulations (Morgan et al., 2021) of SC-mediated coarsening in wild-type Arabidopsis thaliana, we used a per-SC criterion to decide which RIs at the end of the simulation should be designated as crossovers. This criterion was chosen to be a threshold of 40% of the maximum HEI10 amount at those RIs on the same SC. However, this criterion needed to be changed to study nucleoplasmic-mediated coarsening, and a simple absolute threshold would require substantial reparameterization of the HEI10 model.

Instead, we designed a new per-cell criterion. RIs were designated as crossovers if they contained an amount of HEI10 more than 60% of the mean amount of HEI10 at an RI in that cell, where this mean excluded RIs with less HEI10 than an absolute threshold of 1 a.u. A per-cell threshold based on the mean amount rather than the maximum amount was used because of the substantial variation in maximum HEI10 level found in simulations of the *pch-1* mutant. All simulation outputs in this manuscript use this adjusted threshold. We found that this made only a limited change to the results of simulating SC-mediated coarsening in WT and HEI10 overexpressing cells.

Data Availability

Imaging data associated with this study are available at doi.org/10.6084/m9.figshare.19650249.v1, doi.org/10.6084/m9.figshare.19665810.v1 and doi.org/10.6084/m9.figshare.21989732. Custom Python scripts for data analysis are available at https://github.com/jfozard/hei10_zyp1.

References

Agarwal S, Roeder GS. 2000. Zip3 Provides a Link between Recombination Enzymes and Synaptonemal Complex Proteins. *Cell* **102**:245–255. doi:https://doi.org/10.1016/S0092-8674(00)00029-5

741 Arshadi C, Günther U, Eddison M, Harrington KIS, Ferreira TA. 2021. SNT: a unifying toolbox for
742 quantification of neuronal anatomy. *Nat Methods* **18**:374–377. doi:10.1038/s41592-021-
743 01105-7

744 Ball G, Demmerle J, Kaufmann R, Davis I, Dobbie IM, Schermelleh L. 2015. SIMcheck: a Toolbox for
745 Successful Super-resolution Structured Illumination Microscopy. *Sci Rep* **5**:15915.
746 doi:10.1038/srep15915

747 Bhalla N. 2022. PCH-2 and meiotic HORMADs: A module for evolutionary innovation in
748 meiosis?Current Topics in Developmental Biology. Academic Press.
749 doi:https://doi.org/10.1016/bs.ctdb.2022.07.001

750 Cameron AC, Trivedi PK. 1990. Regression-based tests for overdispersion in the Poisson model. *J*
751 *Econom* **46**:347–364. doi:https://doi.org/10.1016/0304-4076(90)90014-K

752 Capilla-Pérez L, Durand S, Hurel A, Lian Q, Chambon A, Taochy C, Solier V, Grelon M, Mercier R.
753 2021. The synaptonemal complex imposes crossover interference and heterochiasmy in
754 Arabidopsis. *Proceedings of the National Academy of Sciences* **118**:e2023613118.
755 doi:10.1073/pnas.2023613118

756 Chelysheva L, Vezon D, Chambon A, Gendrot G, Pereira L, Lemhemdi A, Vrielynck N, le Guin S,
757 Novatchkova M, Grelon M. 2012. The Arabidopsis HEI10 is a new ZMM protein related to Zip3.
758 *PLoS Genet*. doi:10.1371/journal.pgen.1002799

759 Colaiácovo MP, MacQueen AJ, Martinez-Perez E, McDonald K, Adamo A, la Volpe A, Villeneuve AM.
760 2003. Synaptonemal Complex Assembly in C. elegans Is Dispensable for Loading Strand-
761 Exchange Proteins but Critical for Proper Completion of Recombination. *Dev Cell* **5**:463–474.
762 doi:10.1016/S1534-5807(03)00232-6

763 di Marzo GA. 1992. Méthodes de Rosenbrock d'ordre 5(4) adaptées aux problemes différentiels-
764 algébriques.

765 Du G, Drexler GA, Friedland W, Greubel C, Hable V, Krücken R, Kugler A, Tonelli L, Friedl AA, Dollinger
766 G. 2011. Spatial dynamics of DNA damage response protein foci along the ion trajectory
767 of high-LET particles. *Radiat Res* **176**:706–715. doi:10.1667/rr2592.1

768 Durand S, Lian Q, Jing J, Ernst M, Grelon M, Zwicker D, Mercier R. 2022. Joint control of meiotic
769 crossover patterning by the synaptonemal complex and HEI10 dosage. *Nat Commun* **13**:5999.
770 doi:10.1038/s41467-022-33472-w

771 Duroc Y, Lemhemdi A, Larchevêque C, Hurel A, Cuacos M, Cromer L, Horlow C, Armstrong SJ,
772 Chelysheva L, Mercier R. 2014. The Kinesin AtPSS1 Promotes Synapsis and is Required for
773 Proper Crossover Distribution in Meiosis. *PLoS Genet* **10**:e1004674-.

774 Ferdous M, Higgins JD, Osman K, Lambing C, Roitinger E, Mechtler K, Armstrong SJ, Perry R, Pradillo
775 M, Cuñado N, Franklin FCH. 2012. Inter-Homolog Crossing-Over and Synapsis in Arabidopsis
776 Meiosis Are Dependent on the Chromosome Axis Protein AtASY3. *PLoS Genet* **8**:e1002507-.

777 France MG, Enderle J, Röhrig S, Puchta H, Franklin FCH, Higgins JD. 2021. ZYP1 is required for
778 obligate cross-over formation and cross-over interference in Arabidopsis. *Proceedings of the*
779 *National Academy of Sciences* **118**. doi:10.1073/pnas.2021671118

780 Gray S, Cohen PE. 2016. Control of Meiotic Crossovers: From Double-Strand Break Formation to
781 Designation. *Annu Rev Genet*. doi:10.1146/annurev-genet-120215-035111

782 Haldane JBS. 1931. The Cytological Basis of Genetical Interference. *Cytologia (Tokyo)* **3**:54–65.
783 doi:10.1508/cytologia.3.54

784 Hunter N. 2015. Meiotic Recombination: The Essence of Heredity. *Cold Spring Harb Perspect Biol*
785 **7**:a016618. doi:10.1101/cshperspect.a016618

786 Jahns MT, Vezon D, Chambon A, Pereira L, Falque M, Martin OC, Chelysheva L, Grelon M. 2014.
787 Crossover Localisation Is Regulated by the Neddylation Posttranslational Regulatory Pathway.
788 *PLoS Biol* **12**:e1001930-.

789 Jantsch V, Pasierbek P, Mueller MM, Schweizer D, Jantsch M, Loidl J. 2004. Targeted gene knockout
790 reveals a role in meiotic recombination for ZHP-3, a Zip3-related protein in Caenorhabditis
791 elegans. *Mol Cell Biol* **24**:7998–8006. doi:10.1128/MCB.24.18.7998-8006.2004

792 Jones GH, Franklin FCH. 2006. Meiotic Crossing-over: Obligation and Interference. *Cell* **126**:246–248.
793 doi:https://doi.org/10.1016/j.cell.2006.07.010

794 Lake CM, Nielsen RJ, Guo F, Unruh JR, Slaughter BD, Hawley RS. 2015. Vilya, a component of the
795 recombination nodule, is required for meiotic double-strand break formation in Drosophila.
796 *Elife* **4**:e08287. doi:10.7554/eLife.08287

797 Lam WS, Yang X, Makaroff CA. 2005. Characterization of Arabidopsis thaliana SMC1 and SMC3:
798 evidence that AtSMC3 may function beyond chromosome cohesion. *J Cell Sci* **118**:3037–3048.
799 doi:10.1242/jcs.02443

800 Lambing C, Kuo PC, Tock AJ, Topp SD, Henderson IR. 2020. ASY1 acts as a dosage-dependent
801 antagonist of telomere-led recombination and mediates crossover interference in Arabidopsis.
802 *Proceedings of the National Academy of Sciences* **117**:13647–13658.
803 doi:10.1073/pnas.1921055117

804 Lambing C, Osman K, Nuntasoontorn K, West A, Higgins JD, Copenhaver GP, Yang J, Armstrong SJ,
805 Mechtler K, Roitinger E, Franklin FCH. 2015. Arabidopsis PCH2 Mediates Meiotic Chromosome
806 Remodeling and Maturation of Crossovers. *PLoS Genet* **11**:e1005372-.

807 Lloyd A. 2022. Crossover patterning in plants. *Plant Reprod*. doi:10.1007/s00497-022-00445-4

808 Mercier R, Jolivet S, Vezon D, Huppe E, Chelysheva L, Giovanni M, Nogué F, Doutriaux M-P, Horlow C,
809 Grelon M, Mézard C. 2005. Two Meiotic Crossover Classes Cohabit in Arabidopsis: One Is
810 Dependent on MER3,whereas the Other One Is Not. *Current Biology* **15**:692–701.
811 doi:https://doi.org/10.1016/j.cub.2005.02.056

812 Miller DE. 2020. The Interchromosomal Effect: Different Meanings for Different Organisms. *Genetics*
813 **216**:621–631. doi:10.1534/genetics.120.303656

814 Morgan C, Fozard JA, Hartley M, Henderson IR, Bomblies K, Howard M. 2021. Diffusion-mediated
815 HEI10 coarsening can explain meiotic crossover positioning in Arabidopsis. *Nat Commun*
816 **12**:4674. doi:10.1038/s41467-021-24827-w

817 Morgan C, Wegel E. 2020. Cytological Characterization of Arabidopsis arenosa Polyploids by SIM. In:
818 Pradillo M. HS, editor. Plant Meiosis. Methods in Molecular Biology, Vol 2061. Humana, New
819 York, NY. doi:https://doi.org/10.1007/978-1-4939-9818-0_4

820 Otto SP, Payseur BA. 2019. Crossover Interference: Shedding Light on the Evolution of
821 Recombination. *Annu Rev Genet*. doi:10.1146/annurev-genet-040119-093957

822 Page SL, Hawley RS. 2004. THE GENETICS AND MOLECULAR BIOLOGY OF THE SYNAPTONEMAL
823 COMPLEX. *Annu Rev Cell Dev Biol* **20**:525–558. doi:10.1146/annurev.cellbio.19.111301.155141

824 Pochon G, Henry IM, Yang C, Lory N, Jiménez NF-, Böwer F, Hu B, Carstens L, Tsai HT, Pradillo M,
825 Comai L, Schnittger A. 2022. The Arabidopsis Hop1 homolog ASY1 mediates cross-over
826 assurance and interference. *bioRxiv* 2022.03.17.484635. doi:10.1101/2022.03.17.484635

827 Prusicki MA, Keizer EM, van Rosmalen RP, Komaki S, Seifert F, Müller K, Wijnker E, Fleck C, Schnittger
828 A. 2019. Live cell imaging of meiosis in Arabidopsis thaliana. *Elife* **8**:e42834.
829 doi:10.7554/eLife.42834

830 Qiao H, Prasada Rao HBD, Yang Y, Fong JH, Cloutier JM, Deacon DC, Nagel KE, Swartz RK, Strong E,
831 Holloway JK, Cohen PE, Schimenti J, Ward J, Hunter N. 2014. Antagonistic roles of ubiquitin
832 ligase HEI10 and SUMO ligase RNF212 regulate meiotic recombination. *Nat Genet* **46**:194–199.
833 doi:10.1038/ng.2858

834 Rackauckas C, Nie Q. 2017. DifferentialEquations.jl - A performant and Feature-Rich Ecosystem for
835 Solving Differential Equations in Julia. *J Open Res Softw* **5**:15.
836 doi:http://doi.org/10.5334/jors.151

837 Reynolds A, Qiao H, Yang Y, Chen JK, Jackson N, Biswas K, Holloway JK, Baudat F, de Massy B, Wang J,
838 Höög C, Cohen PE, Hunter N. 2013. RNF212 is a dosage-sensitive regulator of crossing-over
839 during mammalian meiosis. *Nat Genet* **45**:269–278. doi:10.1038/ng.2541

840 Rog O, Köhler S, Dernburg AF. 2017. The synaptonemal complex has liquid crystalline properties and
841 spatially regulates meiotic recombination factors. *Elife* **6**:e21455. doi:10.7554/eLife.21455

842 Stauffer WT, Zhang L, Dernburg A. 2019. Diffusion through a liquid crystalline compartment
843 regulates meiotic recombinationProc.SPIE. doi:10.1117/12.2513378

844 Sturtevant AH. 1915. The behavior of the chromosomes as studied through linkage. *Z Indukt*
845 *Abstamm Vererbungsl*. doi:10.1007/BF01792906

846 Termolino P, Falque M, Aiese Cigliano R, Cremona G, Paparo R, Ederveen A, Martin OC, Consiglio FM,
847 Conicella C. 2019. Recombination suppression in heterozygotes for a pericentric inversion
848 induces the interchromosomal effect on crossovers in Arabidopsis. *The Plant Journal* **100**:1163–
849 1175. doi:https://doi.org/10.1111/tpj.14505

850 Varas J, Graumann K, Osman K, Pradillo M, Evans DE, Santos JL, Armstrong SJ. 2015. Absence of
851 SUN1 and SUN2 proteins in Arabidopsis thaliana leads to a delay in meiotic progression and
852 defects in synapsis and recombination. *The Plant Journal* **81**:329–346.
853 doi:https://doi.org/10.1111/tpj.12730

854 von Diezmann L, Rog O. 2021. Let's get physical – mechanisms of crossover interference. *J Cell Sci*
855 **134**. doi:10.1242/jcs.255745

856 Wang S, Veller C, Sun F, Ruiz-Herrera A, Shang Y, Liu H, Zickler D, Chen Z, Kleckner N, Zhang L. 2019.
857 Per-Nucleus Crossover Covariation and Implications for Evolution. *Cell* **177**:326-338.e16.
858 doi:https://doi.org/10.1016/j.cell.2019.02.021

859 Wayne C, Chloe G, Andrew L. 2021. Crossover interference: Just ZYP it. *Proceedings of the National*
860 *Academy of Sciences* **118**:e2103433118. doi:10.1073/pnas.2103433118

861 Yang C, Hu B, Portheine SM, Chuenban P, Schnittger A. 2020. State changes of the HORMA protein
862 ASY1 are mediated by an interplay between its closure motif and PCH2. *Nucleic Acids Res*
863 **48**:11521–11535. doi:10.1093/nar/gkaa527

864 Yang C, Sofroni K, Hamamura Y, Hu B, Elbasi HT, Balboni M, Chu L, Stang D, Heese M, Schnittger A.
865 2022. ZYP1-mediated recruitment of PCH2 to the synaptonemal complex remodels the
866 chromosome axis leading to crossover restriction. *Nucleic Acids Res* **50**:12924–12937.
867 doi:10.1093/nar/gkac1160

868 Zhang L, Köhler S, Rillo-Bohn R, Dernburg AF. 2018. A compartmentalized signaling network
869 mediates crossover control in meiosis. *Elife* **7**:e30789. doi:10.7554/eLife.30789

870 Zhang L, Stauffer W, Zwicker D, Dernburg AF. 2021. Crossover patterning through kinase-regulated
871 condensation and coarsening of recombination nodules. *bioRxiv* 2021.08.26.457865.
872 doi:10.1101/2021.08.26.457865

873 Zickler D, Kleckner N. 2016. A few of our favorite things: Pairing, the bouquet, crossover interference
874 and evolution of meiosis. *Semin Cell Dev Biol*. doi:10.1016/j.semcdb.2016.02.024

875 Ziolkowski PA, Underwood CJ, Lambing C, Martinez-Garcia M, Lawrence EJ, Ziolkowska L, Griffin C,
876 Choi K, Franklin FCH, Martienssen RA, Henderson IR. 2017. Natural variation and dosage of the
877 HEI10 meiotic E3 ligase control Arabidopsis crossover recombination. *Genes Dev*.
878 doi:10.1101/gad.295501.116

879

880

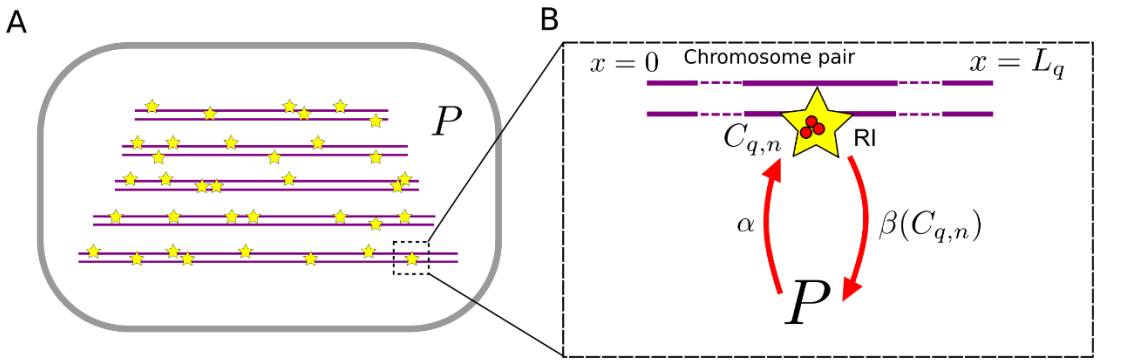

C

Equation System

RIs

$$\frac{\mathrm{d}C_{q,n}}{\mathrm{d}t} = (\alpha P - \beta(C_{q,n})C_{q,n})\, H_s(C_{q,n} - K_H), \qquad 1 \le q \le Q,\ 1 \le n \le N_q,$$

Nucleoplasm

$$\frac{\mathrm{d}P}{\mathrm{d}t} = \sum_{q=1}^{Q}\sum_{n=1}^{N_q} (\beta(C_{q,n})C_{q,n} - \alpha P)\, H_s(C_{q,n} - K_H),$$

Function definitions

$$\beta(C_{q,n}) = \frac{\beta_C}{1 + (C_{q,n}/K_C)^{\gamma}}, \quad H_s(s) = \frac{1}{2}\left(1 + \tanh(K_s s)\right),$$

Initial conditions

$$F = \mathcal{N}_T(\mu_F, \sigma_F^2, -3, 3), \quad \hat{C}_{q,n} = f(x_{q,n}/L_q)\mathcal{N}_T(1, \sigma_C^2, -3, 3),$$

$$C_{q,n}(t=0) = R_{RI} F \frac{\hat{C}_{q,n}}{\sum_{q'=1}^{Q}\sum_{n'=1}^{N_q} \hat{C}_{q',n'}}, \quad P(t=0) = R_P F.$$

D

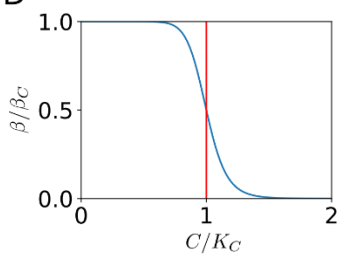

F

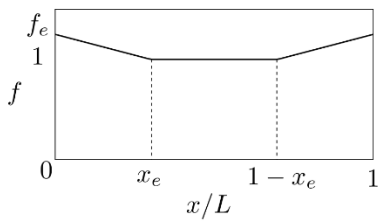

E

α	$0.14\,\mathrm{s}^{-1}$	RI HEI10 absorption rate
β_C	$0.03\,\mathrm{s}^{-1}$	RI HEI10 escape rate
γ	1.25	Escape rate Hill coefficient
K_C	1 au	Hill function threshold
K_H	0.5 au	Smooth switchoff threshold
K_s	$10\,\mathrm{au}^{-1}$	Smooth switchoff sharpness
x_e	0.3	Telomere length (fraction of chromosome pair)
f_e	1.25	Telomere weighting for RI loading
ρ	$0.5\,\mu\mathrm{m}^{-1}$	Average RI density along chromosome pairs
R_{RI}	0.76	Proportion of initial HEI10 loaded at RIs
R_P	0.24	Proportion of initial HEI10 in nucleoplasmic pool
μ_F	1170 au	Mean initial total cellular HEI10 amount
σ_F	75 au	Standard deviation of total initial HEI10 amount
σ_C	0.33	Relative noise in HEI10 RI loading
T	36000 s	Simulation duration
Q	5	Number of chromosome pairs

G

L_q	Length of the q-th chromosome pair
P	Amount of HEI10 in nucleoplasmic pool
$C_{q,n}$	Amount of HEI10 in the n-th RI on the q-th chromosome pair
$x_{q,n}$	Distance of n-th RI along the q-th chromosome pair
q	Chromosome pair index $1 \le q \le Q$
n	RI index along chromosome pair
N_q	Number of RIs on q-th chromosome pair

Figure 1. Mathematical model for HEI10 dynamics in a *zyp1* SC mutant. (**A**) Each cell contains Q=5 chromosome pairs (purple line pairs). RIs (yellow stars) are placed randomly along the chromosome pairs immersed in the nucleoplasm (P). (**B**) HEI10 (red) is able to move from the nucleoplasmic pool into the RI compartments (rate *α*), and escape (rate β) from the RI compartments back into the pool. $C_{q,n}$ is the HEI10 molecule number at the *n*-th RI on the *q*-th chromosome pair, which has length L_q. (**C**) Differential equations governing nucleoplasmic pool (P) and RI HEI10 (C) amounts, together with functional form of escape rate function $\beta(C)$, smoothing function *H(s)* and initial conditions for RI and nucleoplasmic HEI10 amounts. $\mathcal{N}_T$ is a Normal distribution, truncated at three standard deviations away from its mean. (**D**) Graph showing RI escape rate function $\beta(C)$. (**E**) Default simulation parameter values. (**F**) Form of end-bias function f. (**G**) Description of terms appearing in model equations.

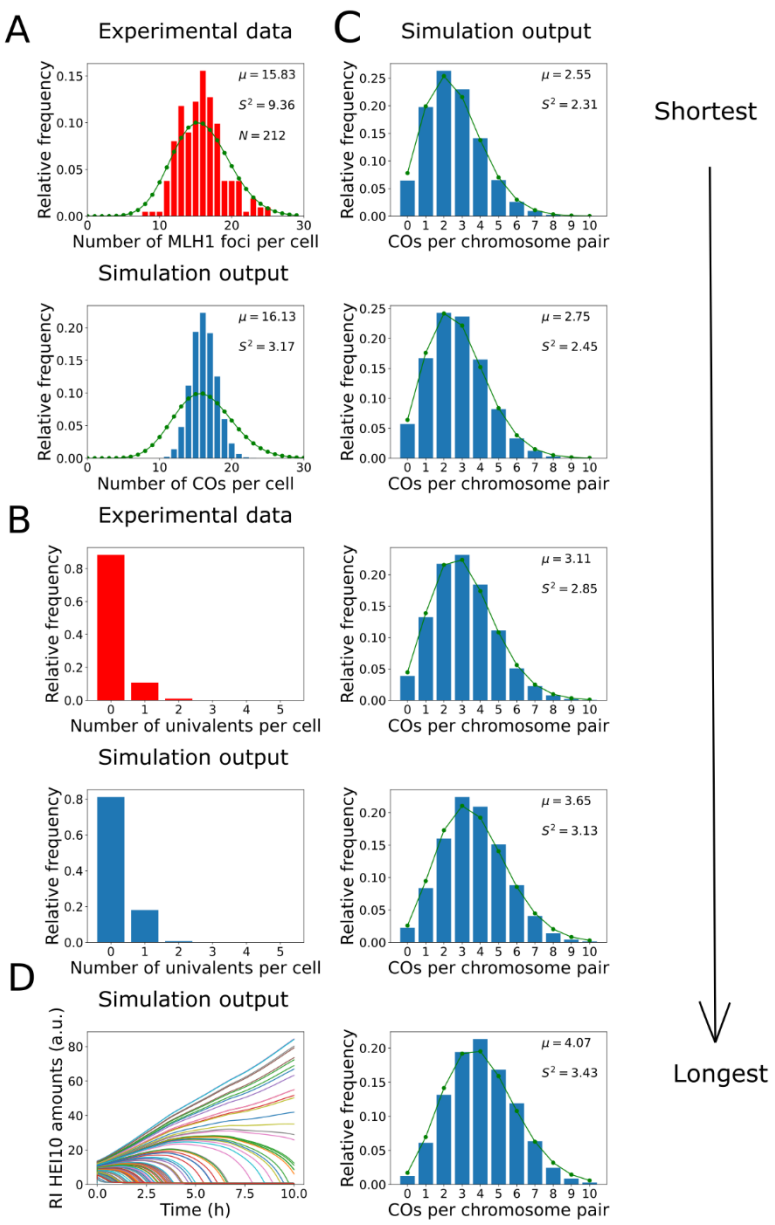

Figure 2. Analysis of CO number in *zyp1* mutant. (A-B) Experimental data from *zyp1* null mutant plants (top) and nucleoplasmic coarsening model simulations (bottom). Results from simulating the model for 10000 cells are shown. (**A**) Distribution of total-CO number per cell. Experimental data is from pooled MLH1 foci counts from (Capilla- Pérez *et al.,* 2021). Sample mean (μ), estimated variance (S^2), and sample size (N) inset. Green dots (joined by a line) show a Poisson distribution with the same mean. (**B**) Distribution of univalent number per cell. Experimental data is from univalent counts in metaphase I chromosomes from (Capilla- Pérez *et al.,* 2021). Again data from 10000 simulated cells (**C**) Simulation outputs showing the distribution of total-CO numbers on the five individual chromosomes pairs. Green dots and lines again show Poisson distributions with same means as simulated data, with sample mean (μ) and estimated variance (S^2) inset. Simulation output from 10000 cells. (**D**) Traces of HEI10 focus intensity against time, for all RIs within a single simulated cell. Coloured lines indicate HEI10 amounts at each RI, in arbitrary units (a.u.). All simulation parameters are listed in Figure 1E.

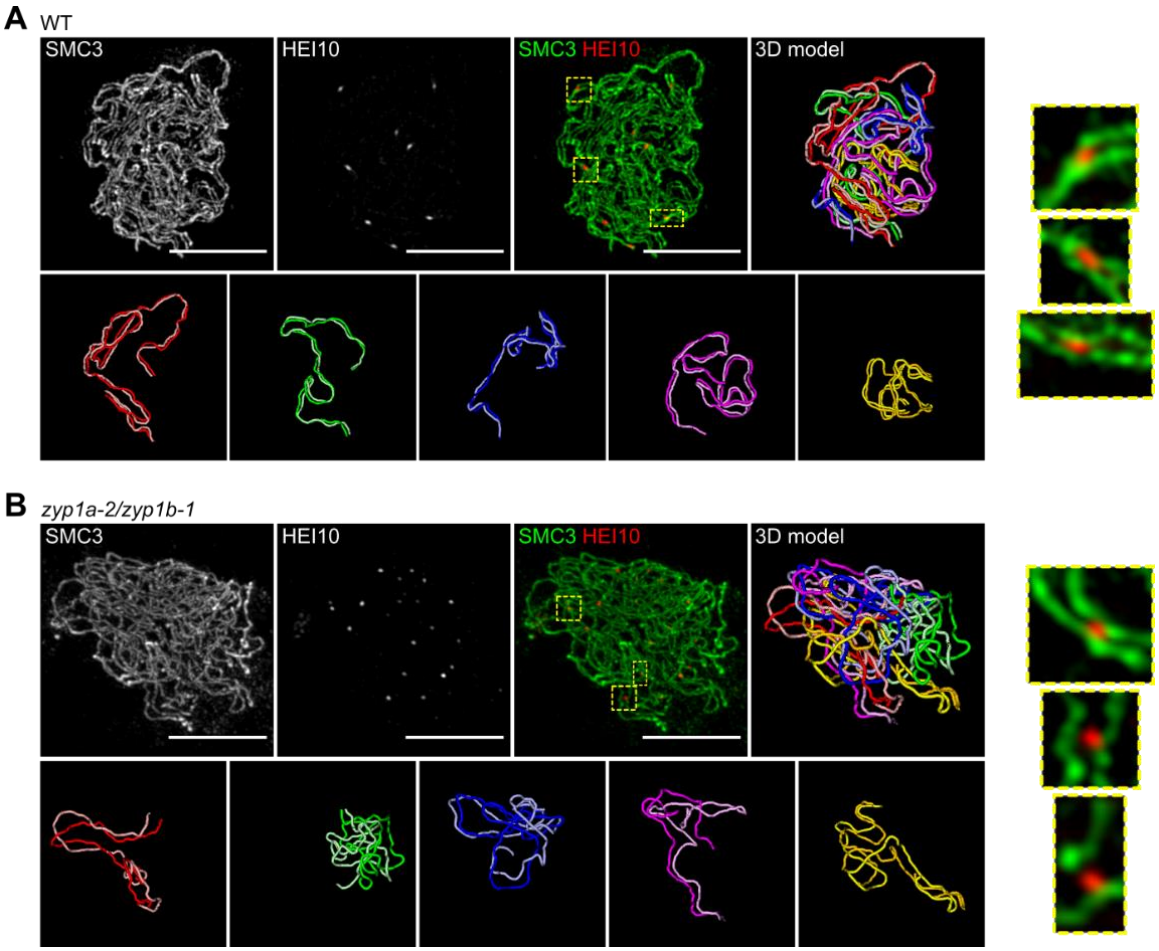

Figure 3. 3D-SIM imaging of late-prophase I cells. Maximum intensity projections of 3D-image stacks from wild-type (**A**) and *zyp1a-2/zyp1b-1* mutants (**B**), labelled for SMC3 (green) and HEI10 (red). 3D-models of segmented axial elements (with each chromosome axis labelled in a different colour), generated using the SNT plugin to FIJI, are also shown. Each nucleus contains 5 pairs of axes (bottom row, A, B), with individual axes in each pair having equivalent lengths and pairing tightly (A) or roughly (B) in 3D space. Zoomed in regions (right hand panels) from merged images (yellow dashed boxes) show the localisation of late-HEI10 foci between closely-paired axes. Scale bars = 5 µm.

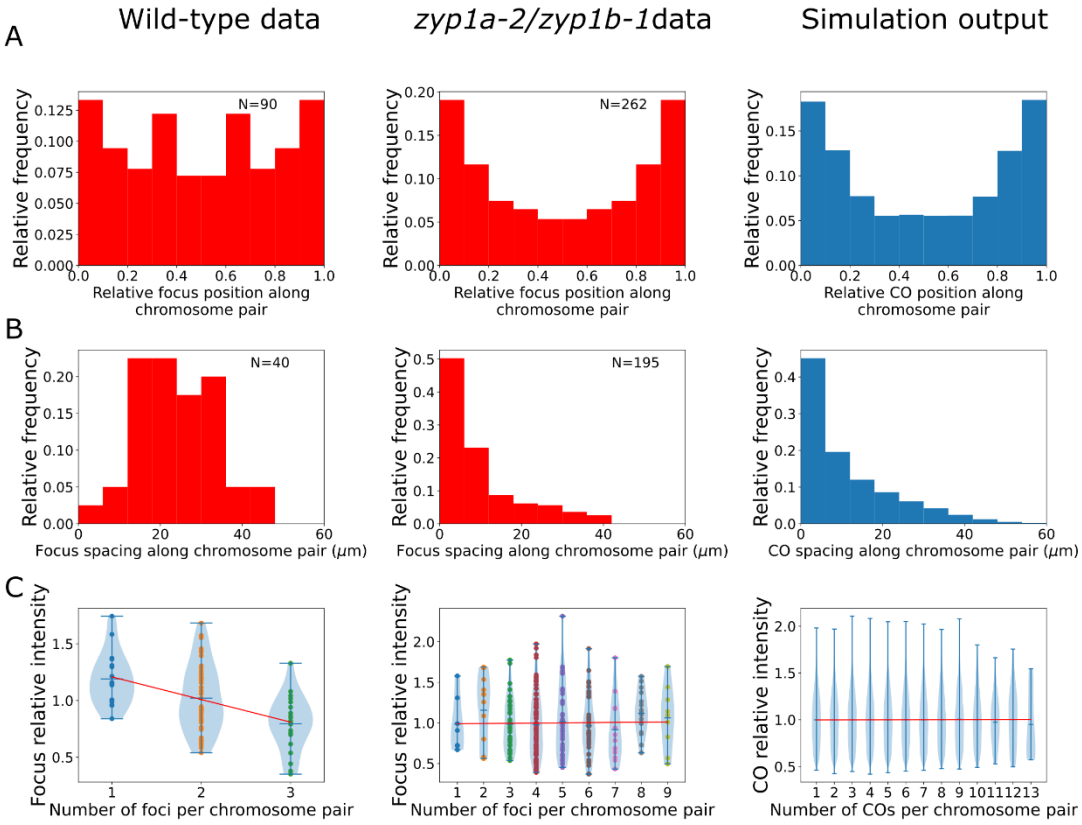

Figure 4. Analysis of late-HEI10 focus patterning and intensity data in wild-type and *zyp1* mutant. **(A-C)** Experimental data from wild-type plants (left), *zyp1a-2/zyp1b-1* plants (middle), and from nucleoplasmic coarsening model simulation outputs (right). Model outputs from simulating 10000 cells are shown. (**A**) Late-HEI10 focus positions along chromosome pairs, relative to the length of the chromosome pair. Experimental data are replicated and made symmetric about chromosome midpoints. (N=161322 simulated foci). (**B**) Distribution of spacing between adjacent late-HEI10 foci, in µm. (N=113278 simulated spaces between foci). (**C**) Violin plots of late-HEI10 foci intensities against the number of late-HEI10 foci on that chromosome pair. Focus intensities are relative to the mean intensity of all (on-chromosome) HEI10 foci within the same cell. Red lines show simple linear regression best fits, treating the number of foci on the chromosome as a continuous independent variable. For wild-type plants, slope = -0.1944, R^2=0.188, F(1,88)=20.36, p<0.001. For *zyp1* mutant plants, slope=0.0028, R^2<0.001, F(1,260)=0.04538, p=0.831. For simulated data, slope=0.0004, R^2<0.001, F(1,161320)=0.7838, p=0.376. Simulation parameters are again as listed in Figure 1E, with simulated data from 10000 cells (50000 chromosome pairs).

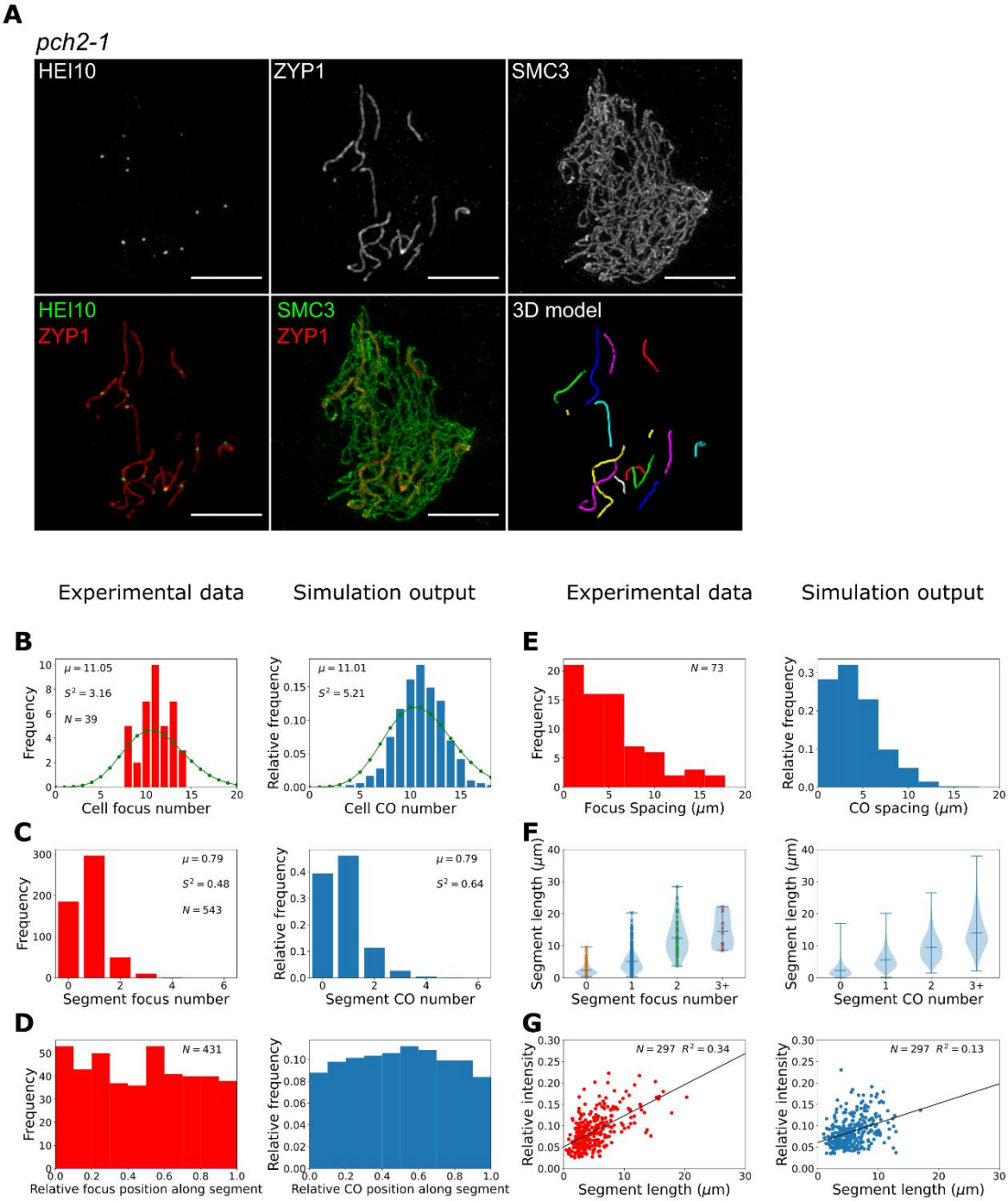

Figure 5. Late-HEI10 focus patterning and intensity data in *pch2-1.* (**A**) Maximum intensity projections of 3D-image stacks from *pch2-1* mutants labelled for HEI10, ZYP1 and SMC3. A 3D-model of segmented SC segments (with each segment labelled in a different colour), generated using the SNT plugin to FIJI, is also shown. (**B-G**) Experimental data and combined coarsening model simulations showing; (**B**) late-HEI10 focus number per cell (1000 simulated cells), green dots (joined by a line) show a Poisson distribution with the same mean, (**C**) late-HEI10 focus number per SC segment (13870 simulated segments), (**B-C**) sample mean (μ) and estimated variance (S^2) inset, (**D**) positioning of all late-HEI10 foci along SC segments relative to total segment length (11009 simulated foci), (**E**) spacing between neighbouring late-HEI10 foci on the same SC segment (2590 spaces between simulated foci), (**F**) SC segment length versus number of late-HEI10 foci per SC segment (same number of observations as in C) and (**G**) single late-HEI10 focus intensity (relative to

948 the mean intensity of all HEI10 foci within the same cell) versus SC segment length, with a random
949 sample of simulation output to match experimental dataset size.

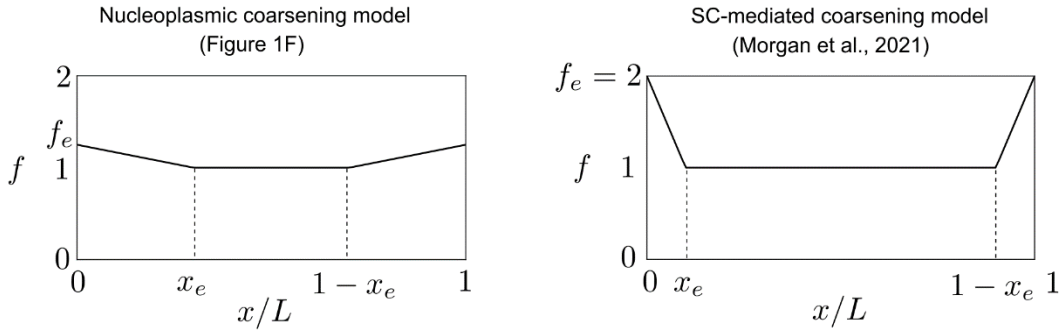

Figure 1 – figure supplement 1. Form of end-bias function f from nucleoplasmic coarsening model (Figure 1F) and from the SC-mediated coarsening model (Morgan et al., 2021). Note that the extra HEI10 loading in the nucleoplasmic coarsening model (up to 25% on the most distal 60% of each chromosome pair) is lower and more spread than that used in the SC-mediated coarsening model (up to 100% on the most distal 20%). Here x/L is relative position along chromosome pair, with x_e = 0.3 (left) and x_e = 0.1 (right), specifying starting position of end-bias, where f_e = 1.25 (left) and f_e = 2 (right).

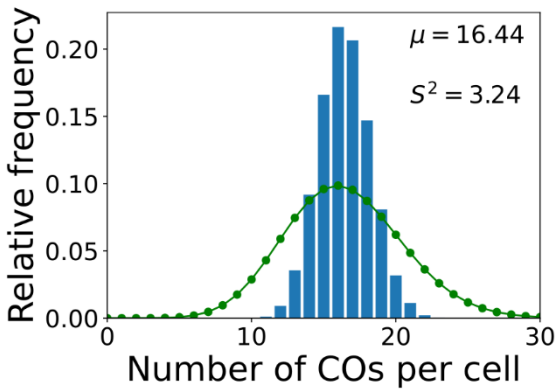

Figure 2 – figure supplement 1. *zyp1* total-CO number per cell simulation without nonuniform initial loading. *zyp1* nucleoplasmic coarsening model simulation showing the distribution of total-CO number per cell, where the model has uniform initial loading (no end-bias). Results from simulating the model for 10000 cells are shown. Sample mean (μ) and estimated variance (S^2) inset. Green dots (joined by a line) show a Poisson distribution with the same mean.

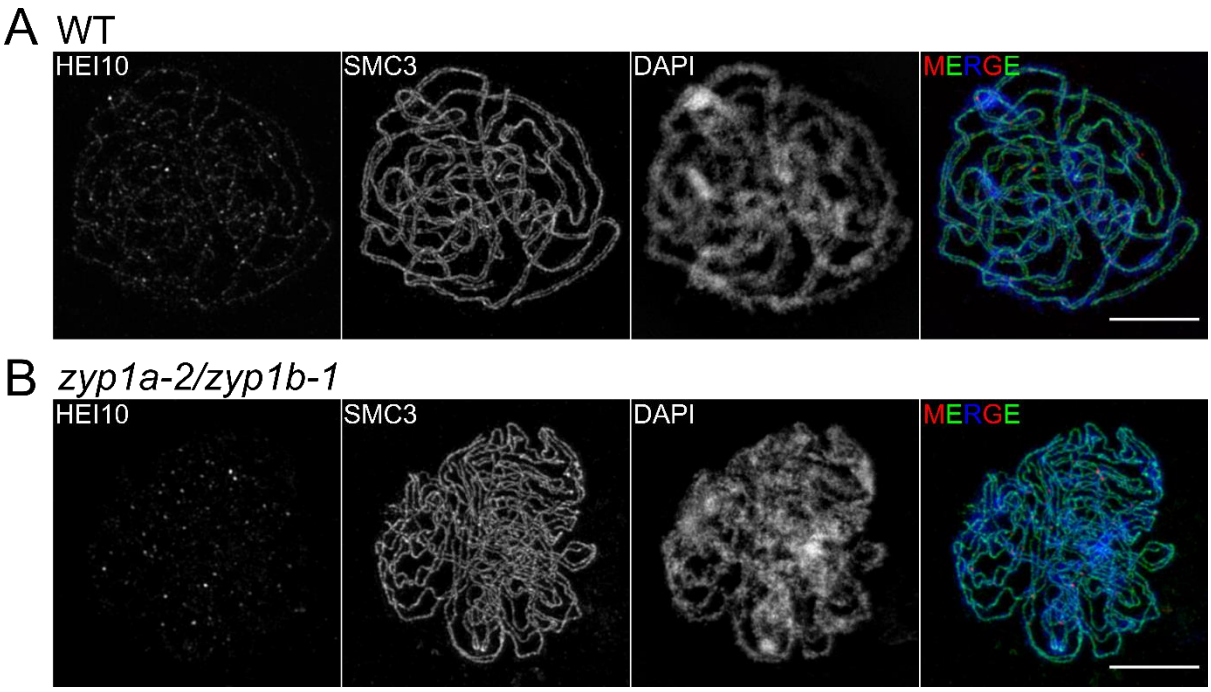

965

966 **Figure 3 – figure supplement 1. 3D-SIM imaging of early pachytene cells**. Maximum intensity
967 projections of 3D-image stacks from wild-type (**A**) and *zyp1a-2/zyp1b-1* mutants (**B**), labelled for
968 HEI10 (red), SMC3 (green) and DAPI (blue). Scale bars = 5 µm.

969

A

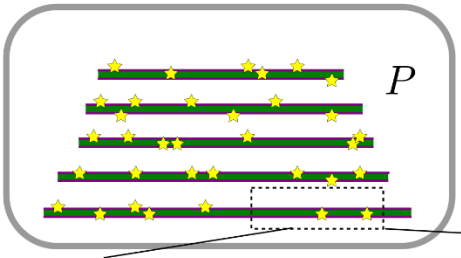

B

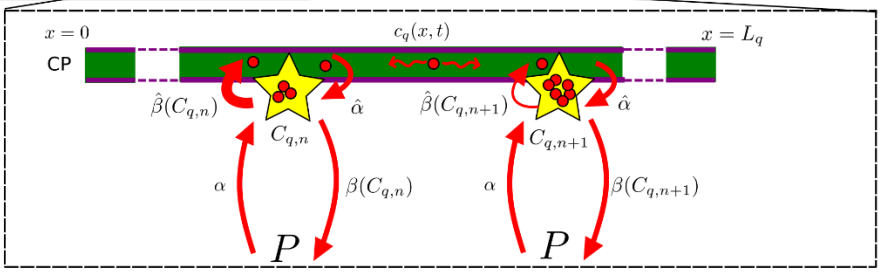

C Equation System

SCs
$$\frac{\partial c_q}{\partial t} = D\frac{\partial^2 c_q}{\partial x^2} + \sum_{n=1}^{N_q} H_s(C_{q,n} - K_H)\left(\hat{\beta}(C_{q,n})C_{q,n} - \hat{\alpha}c_q(x_{q,n})\right)\delta(x - x_{q,n}), \quad 1 \le q \le Q,\ 0 \le x \le L_q,$$

RIs
$$\frac{\mathrm{d}C_{q,n}}{\mathrm{d}t} = H_s(C_{q,n} - K_H)\left\{\alpha P - \beta(C_{q,n})C_{q,n} + \hat{\alpha}c_q(x_{q,n}) - \hat{\beta}(C_{q,n})C_{q,n}\right\}, \quad 1 \le q \le Q,\ 1 \le n \le N_q,$$

Nucleoplasm
$$\frac{\mathrm{d}P}{\mathrm{d}t} = \sum_{q=1}^{Q}\sum_{n=1}^{N_q} H_s(C_{q,n} - K_H)\left\{\beta(C_{q,n})C_{q,n} - \alpha P\right\},$$

Boundary conditions at SC ends
$$\frac{\partial c_q}{\partial x} = 0 \quad \text{at } x = 0 \text{ and } x = L_q, \quad 1 \le q \le Q.$$

Function definitions
$$\beta(C_{q,n}) = \frac{\beta_C}{1 + (C_{q,n}/K_C)^\gamma},\ \hat{\beta}(C_{q,n}) = \frac{\hat{\beta}_C}{1 + (C_{q,n}/K_C)^\gamma},\ H_s(s) = \frac{1}{2}\left(\tanh(sK_s) + 1\right),$$

Initial conditions
$$F = \mathcal{N}_T(\mu_F, \sigma_F^2, -3, 3), \quad \hat{C}_{q,n} = f(x_{q,n}/L_q)\mathcal{N}_T(1, \sigma_C^2, -3, 3),$$
$$C_{q,n}(t=0) = R_{RI}F\frac{\hat{C}_{q,n}}{\sum_{q'=1}^{Q}\sum_{n'=1}^{N_q}\hat{C}_{q',n'}}, \quad c_q(t=0) = \frac{R_{SC}F}{\sum_{q'=1}^{Q}L_{q'}}, \quad P(t=0) = 0$$

D

	WT	WT+nuc	Unit	Description
D	1.1	1.1	$\mu\mathrm{m}^2\mathrm{s}^{-1}$	HEI10 diffusion coefficent on SC
α	0	0.014	s^{-1}	RI HEI10 absorption rate from nucleoplasm
β_C	0	0.003	s^{-1}	RI HEI10 escape rate into nucleoplasm
$\hat{\alpha}$	2.1	1.89	$\mu\mathrm{m}\,\mathrm{s}^{-1}$	RI HEI10 absorption rate from SC
$\hat{\beta}_C$	0.5	0.45	s^{-1}	RI HEI10 escape rate onto SC
γ	1.25	1.25		Escape rate Hill coefficient
K_C	1	1	au	Hill function threshold
K_H	0.5	0.5	au	Smooth switchoff threshold
K_s	10	10	au^{-1}	Smooth switchoff sharpness
x_e	0.1	0.1		Telomere length (fraction of chromosome pair)
f_e	2.0	2.0		Telomere weighting for RI loading
ρ	0.5	0.5	$\mu\mathrm{m}^{-1}$	Average RI density along chromosome pairs
R_{RI}	0.76	0.76		Proportion of initial HEI10 loaded at RIs
R_{SC}	0.24	0.24		Proportion of initial HEI10 on SCs
μ_F	1170	1170	au	Mean initial total cellular HEI10 amount
σ_F	75	75	au	Standard deviation of total initial HEI10 amount
σ_C	0.33	0.33	au	Relative noise in HEI10 RI loading
T	36000	36000	s	Simulation duration
Q	5	5		Number of chromosome pairs

E

L_q	Length of the q-th chromosome pair
P	Amount of HEI10 in nucleoplasmic pool
$C_{q,n}$	Amount of HEI10 in the n-th RI on the q-th chromosome pair
$c_q(x)$	Amount of HEI10 per unit length on the q-th chromosome pair
x	Distance along the chromosome pair
$x_{q,n}$	Distance of n-th RI along the q-th chromosome pair
q	Chromosome pair index $1 \le q \le Q$
n	RI index along chromosome pair
N_q	Number of RIs on q-th chromosome pair

Figure 4 – figure supplement 1. A combined SC- and nucleoplasm-mediated coarsening model. (**A**) Schematic representation of the combined coarsening model. **(B)** HEI10 (red) is able to move from the nucleoplasmic pool into the RI compartments (rate α), and escape (rate β) from the RI compartments back into the nucleoplasm. HEI10 can also move from SC compartments into the RI compartments (rate $\hat{\alpha}$) and escape back onto the SC (rate $\hat{\beta}$). HEI10 on the SC has concentration

$c_q(x,t)$, and is able to diffuse along the SC with one-dimensional diffusion coefficient D. $C_{q,n}$ is the HEI10 molecule number at the *n*-th RI on the *q*-th chromosome pair, which has length L_q. (**C**) Differential equations and initial/boundary conditions governing simulations. (**D**) Default simulation parameter values for various scenarios: WT, original SC-mediated coarsening model with wild-type parameters (as implemented in Methods), WT+nuc, combined SC- and nucleoplasm-mediated coarsening model with wild-type parameters. (**E**) Description of terms appearing in model equations.

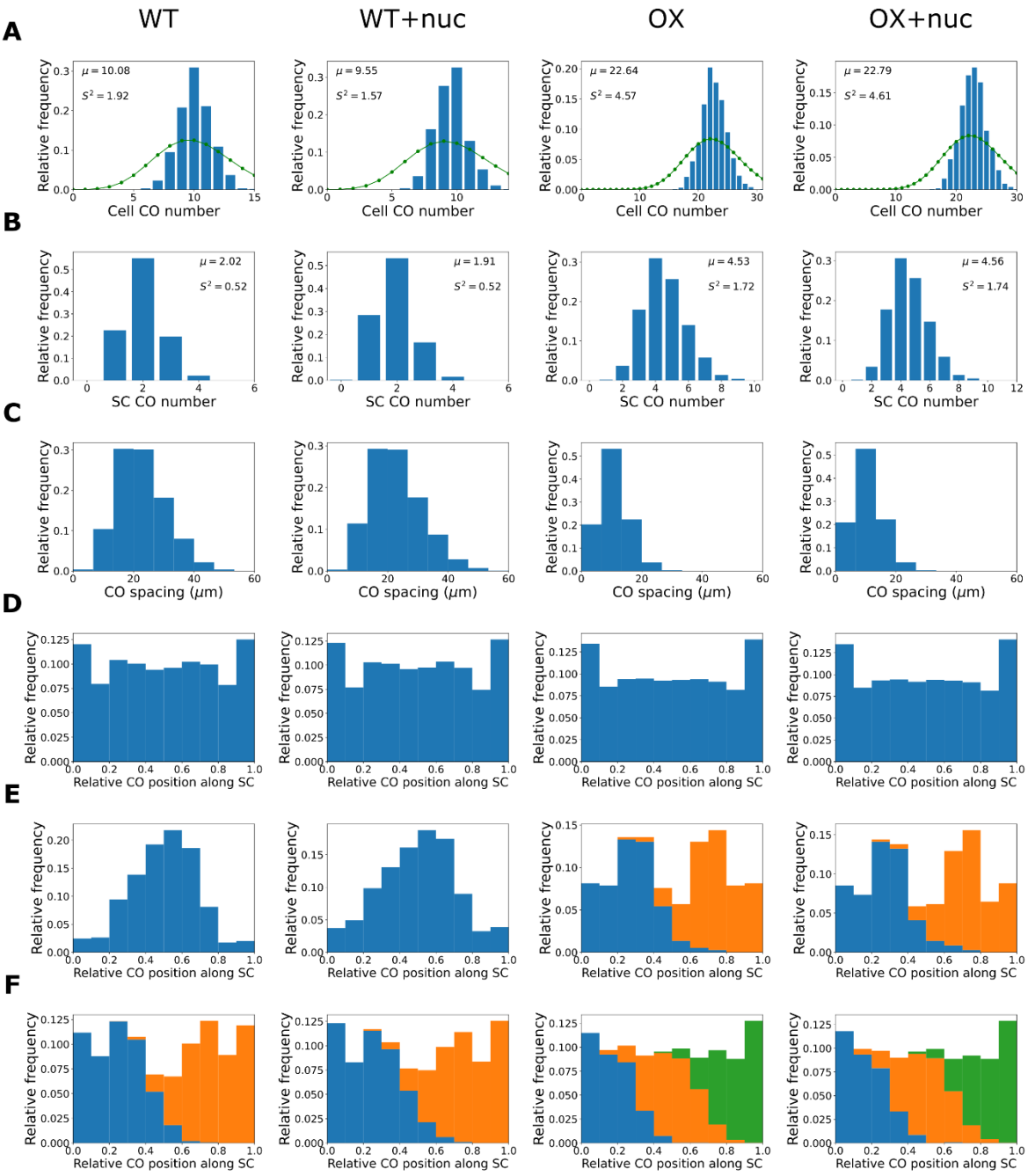

Figure 4 – figure supplement 2. The combined SC- and nucleoplasm-mediated coarsening model can explain crossover patterning in wild-type and HEI10 over-expressor lines. Columns show simulated results from the original SC-mediated coarsening model with wild-type parameters (WT, as implemented in Methods), the combined SC- and nucleoplasm-mediated coarsening model with wild-type parameters (WT+nuc), the original SC-mediated coarsening model with HEI10 over-expressor parameters (OX, as implemented in Methods), and the combined SC- and nucleoplasm-mediated coarsening model with HEI10 over-expressor parameters (OX+nuc). Results from simulating the model for 1000 cells are shown. Above simulations of WT and OX cases agree well with previously published experimental data (Morgan et al., 2021). Number of late-HEI10 foci per cell, green dots (joined by a line) show a Poisson distribution with the same mean, **(A),** number of late-HEI10 foci per SC (5000 simulated SC), **(B)**, sample mean (μ) and estimated variance (S^2) inset

995 (**A-B**), spacing between successive late-HEI10 foci **(C)**, relative positions of late-HEI10 foci along SC
996 **(D)**, relative positions of single late-HEI10 foci (WT, WT+nuc) and double late-HEI10 foci (OX,
997 OX+nuc) **(E)**, and relative positions of double late-HEI10 foci (WT, WT+nuc) and triple late-HEI10 foci
998 (OX, OX+nuc) **(F)**. Parameters are as listed in Figure 4 – figure supplement 1D, with parameters μ_F
999 and σ_F controlling initial cellular HEI10 levels increased to 4.5x the WT values in the HEI10 over-
1000 expressor simulations.

A

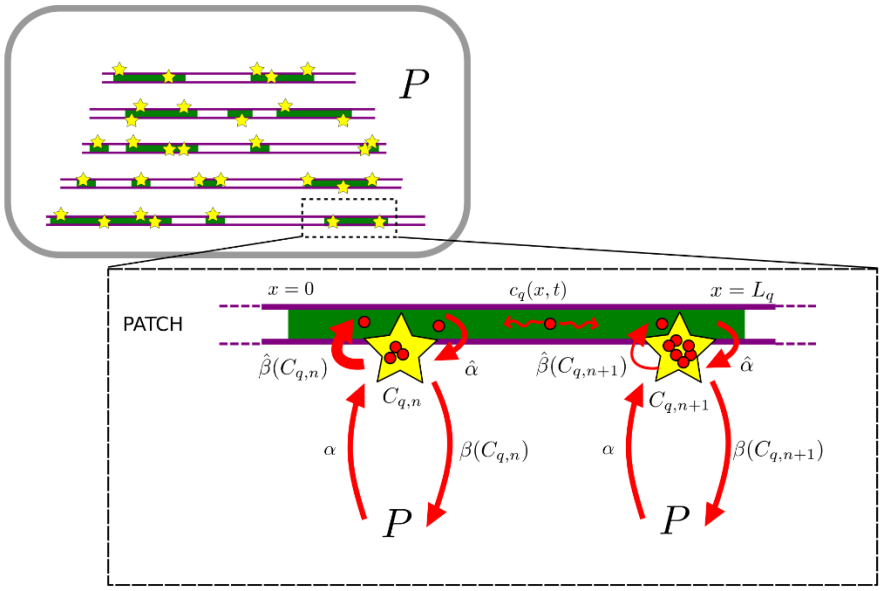

C

	Value	Unit	Description
α	0.014	s^{-1}	RI HEI10 absorption rate from nucleoplasm
β_C	0.003	s^{-1}	RI HEI10 escape rate into nucleoplasm
$\hat{\alpha}$	0.42	$\mu m\, s^{-1}$	RI HEI10 absorption rate from SC
$\hat{\beta}_C$	0.075	s^{-1}	RI HEI10 escape rate onto SC
f_e	1.0		Telomere weighting for RI loading
μ_Q	13.92		Mean number of SC patches
L_α	1.693		Alpha parameter of patch length gamma distribution
L_θ	2.984	μm	Theta parameter of patch length gamma distribution

Figure 5 – figure supplement 1. Model for *pch2* simulations. (**A-B**) Schematic of combined nucleoplasmic- and SC-mediated coarsening model used for *pch2* simulations, where dynamics occur on patches of SC, rather than whole chromosomes. (**C**) Parameters for *pch2* simulations that are different from those in Figure 4 – figure supplement 1D. See Methods for more details.